Thesis for the degree
Master of Science

Submitted to the Scientific Council of the
Weizmann Institute of Science
Rehovot, Israel

עבודת גמר (תזה) לתואר
מוסמך למדעים

מוגשת למועצה המדעית של
מכון ויצמן למדע
רחובות, ישראל

By
Yoav Levine

מאת
יואב לוין

מימוש מצבי צבירה טופולוגיים עם סריגים על-מוליכים

Realizing Topological Phases with Superconducting Lattices

Advisor:
Prof. Yuval Oreg

מנחה:
פרופ' יובל אורג

January 2017

טבת התשע"ז

Abstract

The realization of topological superconductors (SCs) in one or two dimensions is a highly pursued goal. Prominent proposed realization schemes for these phases include semiconductor/superconductor heterostructures and set stringent constraints on the chemical potential of the system. The ability to keep the chemical potential in the required range while in the presence of an adjacent SC and its accompanied screening effects, is yet to be demonstrated in two-dimensional systems. In this work, we introduce a SC lattice in which the SC is deposited periodically on a one- or two-dimensional sample. We demonstrate that a SC lattice is a practical realization platform for a variety of topological SC phases, which overcomes the challenge of controlling the chemical potential. We show how zero-energy Majorana modes emerge at the ends of a one-dimensional system proximity coupled to a one-dimensional SC lattice, and continue to present SC lattice based realizations of two-dimensional topological phases. We show how one can stabilize a $p_x + ip_y$ SC with chiral zero-energy Majorana modes at its edges and obtain signatures of the gapless topological SC phase. In particular, we establish that even when assuming the worst case of absolute screening, in which the chemical potential under the SC is completely unaffected by the external gate potential, all of the above described topological phases can be achieved by tuning the chemical potential in the areas not covered by the SC.

Contents

Chapter 1

Introduction

1.1 Topological Superconductors and Majoranas

Topological superconductivity is a state of matter that received much attention in recent years, mostly because it is associated with quasiparticle excitations which are Majorana fermions. It is still unclear if there are elementary particles which are Majorana fermions, but they are likely to exist as quasiparticle excitations in certain condensed matter systems. In these systems, the analog of a Majorana fermion is a collective excitation of elementary particles, that has zero energy and is self conjugate. We will refer to these zero energy Majorana fermion modes as "zero-energy Majorana modes" or simply as "Majorna modes" throughout this thesis. These Majorana modes are especially interesting due to their special exchange statistics: They are non-abelian anyons [1]. This means, that unlike other known particle types where an exchange operation merely has the effect of multiplying the wavefunction by a scalar factor, exchanges of Majorana modes are nontrivial operations which in general do not commute. As they are excitations of a topological phase, Majorana modes often present themselves as gapless excitations that reside at the edges of systems with gapped bulk spectrums. This gap protects the excitation in the sense that in order to destroy the topological phase and become a trivially gapped system without zero energy excitations, the gap must close. Their non abelian braiding properties, together with their topological protection and their ability to store non-local quantum information, has placed Majorana modes as a promising condensed matter candidate for the realization of fault tolerant quantum computation [2, 3, 4].

Being its own anti-particle means that a zero energy Majorana mode must be an equal superposition of an electron and a hole state. It is natural to search for such excitations in superconducting systems, where the wavefunctions of Boguliubov quasiparticles have both an electron and a hole component. However, the annihilation operator of a quasiparticle in an ordinary s-wave SC has the form $b = uc^{\dagger}_{\uparrow} + vc_{\downarrow}$, where c_s annihilates a normal fermion with spin projection $s = \uparrow / \downarrow$. This annihilation operator is non-hermitian for any u, v due to the fermion's spin structure. A SC with a "spin-less" form is required, with excitation of: $b = uc^{\dagger} + vc$, where $v = u^*$ would yield a self adjoint creation/ annihilation operator. Kitaev [5] showed that indeed a one-dimensional SC made out of spinless electrons may host bound states that are zero-energy self adjoint Majorana modes at its two ends.

In practice, electrons have spin, and so the realization of Kitaev's spinless SC in a physical system is not straightforward. However, it has been shown that several electronic systems can effectively behave as a spinless SC (or a topological SC), due to a combination of Zeeman splitting, spin-orbit coupling (SOC), and proximity-induced s-wave superconductivity [6, 7, 8, 9, 10]. Experimentally, several groups reported features consistent with Majorana end modes in a variety of systems composed of semiconductor/SC heterostructures [11, 12, 13, 14, 15, 16, 17].

We shall briefly review the proposal for realization of topological superconductivity in semiconducting one-dimensional

nanowires and semiconducting two-dimensional electron gases (2DEGs).

1.2 1D Majorana Realization

Consider a one-dimensional semiconducting nanowire with Rashba SOC, coupled to a conventional s-wave SC, placed in an external magnetic field in the direction of the wire. The Hamiltonian of the system is given by:

$$H = \int dx \psi_s^\dagger(x) \left[-\frac{\partial_x^2}{2m} - \mu + i\alpha\partial_x\sigma_y + V_Z\sigma_x \right] \psi_{s'}(x) + \left(\Delta\psi_\uparrow^\dagger(x)\psi_\downarrow^\dagger(x) + \text{H.c.} \right), \tag{1.1}$$

where m is the effective electron mass, α is the Rashba SOC constant, V_Z is the Zeeman coupling due to the applied magnetic field, μ is the chemical potential and Δ is the induced pairing potential as a result of the superconducting proximity effect. σ_j are Pauli matrices that act on the spin degree of freedom of ψ. Here and throughout the rest of the thesis, we set $\hbar = 1$. This Hamiltonian can be written in momentum space:

$$\begin{aligned} H &= \int dk \Psi_k^\dagger H_{BDG} \Psi_k \\ H_{BDG} &= \left(\tfrac{k^2}{2m} - \mu - \alpha k\sigma_y \right)\tau_z + V_Z\sigma_x + \Delta\tau_x \\ \Psi_k &= \begin{pmatrix} \psi_{k\uparrow} & \psi_{k\downarrow} & \psi_{-k\downarrow}^\dagger & -\psi_{-k\uparrow}^\dagger \end{pmatrix}^T, \end{aligned} \tag{1.2}$$

where τ_j the Pauli matrices that act on the particle-hole degree of freedom. To show how this model can effectively resemble a spinless SC, we add each of the necessary ingredients one by one and examine their contribution. Without a Zeeman field, SOC and superconductivity, the spectrum of the wire is given by a spin-degenerate parabolic dispersion (Fig. 1.1a). Applying a Zeeman field would split the two spin bands (Fig. 1.1b), which for $-V_Z < \mu < V_Z$ removes spin degeneracy from the Fermi level. At this point electrons seem effectively spinless, however a conventional s-wave SC does not induce pairing between electrons of the same physical spin. The SOC term solves this, rotating the spins at the Fermi points in opposite directions (Fig. 1.1c). Finally, coupling to a conventional s-wave SC induces pairing of electrons from a single band. If the induced pairing term is small compared to the splitting between the bands, we can project out the upper band, remaining with a single nondegenerate band and thus realizing an effective spinless SC.

Beyond the limit of small pairing, by squaring the Hamiltoinian in Eq. (1.2) twice, we can obtain the bulk energy spectrum of the system:

$$E_k = \pm\sqrt{\left(\frac{k^2}{2m} - \mu\right)^2 + (\alpha k)^2 + V_Z^2 + \Delta^2 \pm 2\sqrt{\left[V_Z^2 + (\alpha k)^2\right]\left(\frac{k^2}{2m} - \mu\right)^2 + V_Z^2\Delta^2}}. \tag{1.3}$$

For non-vanishing SOC and induced SC, the gap closes only at $k = 0$ when $\mu^2 + \Delta^2 - V_Z^2 = 0$. This equation defines a surface in the parameter space representing a phase transition surface, as the topological phase can not turn trivial without gap closure. For $\mu = 0$ and $\Delta \ll V_Z$ we have argued that the model is effectively a spinless SC, thus it hosts zero energy Majorana bound states at its ends. Therefore, one concludes that for $\mu^2 < \mu_C^2$ the system is topological and for $\mu^2 > \mu_C^2$ it is trivially gapped, with:

$$\mu_C^2 = V_Z^2 - \Delta^2. \tag{1.4}$$

1.3 2D Majorana Realization

Using the above described ingredients, the topological superconducting phase can be realized in two dimensions [8, 18, 19, 20], namely the $p_x + ip_y$ SC. We analyze the Hamiltonian of a Rashba SOC 2DEG on the $x-y$ plane, with a magnetization

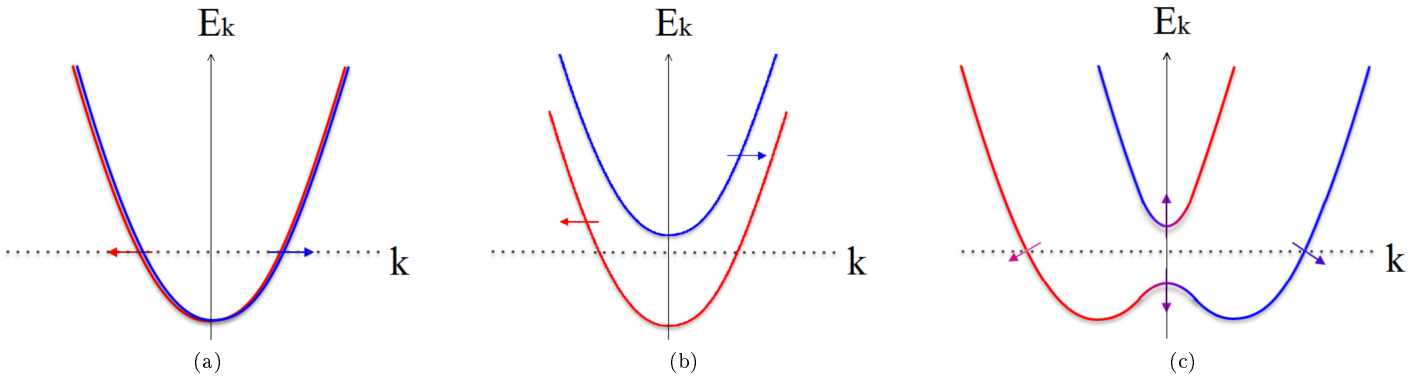

Figure 1.1: Spectrum of the Hamiltonian in Eq. 1.2 before considering induced superconductivity. (a) In the absence of Zeeman field and SOC, the parabolic spectrum is doubly degenerate. (b) Applying a magnetic field, causes the spectrum to split into two opposite-spin bands due to Zeeman coupling. (c) Upon considering spin-orbit coupling, the states on the Fermi level acquire an anti-aligned spin component. Pairing of electrons in a single nondegenerate band is enabled by induced superconductivity from a conventional s-wave SC. Thus, the system behaves as a topological spinless SC near the Fermi level.

term in the $\hat{z}$ direction:

$$H_0 = \int d^2 r \psi_s^\dagger \left(\vec{r}\right) \left[-\frac{\nabla^2}{2m} - \mu - i\alpha \left(\partial_y \sigma_x - \partial_x \sigma_y\right) + V_{\mathrm{Z}} \sigma_z \right] \psi_{s'} \left(\vec{r}\right), \tag{1.5}$$

where m, α, V_{Z}, and μ represent the same quantities as in the one-dimensional case. In this two-dimensional setup, The Rashba terms above can be viewed as an effective magnetic field that aligns the spins in the 2DEG plane, normal to their momentum. The addition of a Zeeman term to the SOC separated bands results in an avoided crossing which resembles a gapped Dirac point at small momenta (Fig. 1.2). Similarly to the one-dimensional case, for $|\mu| < |V_{\mathrm{Z}}|$ the electrons in the quantum well occupy only the lower band and exhibit a single Fermi surface. The Hamiltonian in Eq. (1.5) can be diagonalized in momentum space:

$$H_0 = \int d^2 k \left[E_+ \left(k\right) \psi_+^\dagger \left(\vec{k}\right) \psi_+ \left(\vec{k}\right) + E_- \left(k\right) \psi_-^\dagger \left(\vec{k}\right) \psi_- \left(\vec{k}\right) \right], \tag{1.6}$$

where $\psi_\pm$ annihilate states in the upper/lower bands and obey [20]:

$$\begin{aligned} \psi \left(\vec{k}\right) &= \phi_+ \left(\vec{k}\right) \psi_+ \left(\vec{k}\right) + \phi_- \left(\vec{k}\right) \psi_- \left(\vec{k}\right) \\ \phi_+ \left(\vec{k}\right) &= \begin{pmatrix} A_\uparrow \left(k\right) \\ A_\downarrow \left(k\right) \frac{ik_x - k_y}{k} \end{pmatrix} \\ \phi_- \left(\vec{k}\right) &= \begin{pmatrix} B_\uparrow \left(k\right) \frac{ik_x + k_y}{k} \\ B_\downarrow \left(k\right) \end{pmatrix}, \end{aligned} \tag{1.7}$$

and the energies are given by:

$$E_\pm \left(k\right) = \frac{k^2}{2m} - \mu \pm \sqrt{V_{\mathrm{Z}}^2 + \left(\alpha k\right)^2}. \tag{1.8}$$

The addition of an s-wave SC adds a pairing term that is generated via the proximity effect:

$$H_{SC} = \int d^2r \left[\Delta\psi_\uparrow^\dagger(\vec{r})\,\psi_\downarrow^\dagger(\vec{r}) + \text{H.c.}\right], \tag{1.9}$$

which can be rewritten in momentum space in terms of $\psi_\pm$ as:

$$H_{SC} = \int d^2k \left[\Delta_{+-}(k)\psi_+^\dagger\left(\vec{k}\right)\psi_-^\dagger\left(-\vec{k}\right) + \Delta_{--}(k)\psi_-^\dagger\left(\vec{k}\right)\psi_-^\dagger\left(-\vec{k}\right) + \Delta_{++}(k)\psi_+^\dagger\left(\vec{k}\right)\psi_+^\dagger\left(-\vec{k}\right) + H.c.\right], \tag{1.10}$$

where using Eq. (1.7):

$$\begin{aligned} \Delta_{+-}(k) &= f_s(k)\,\Delta \\ \Delta_{--}(\vec{k}) &= f_p(k)\left(\tfrac{k_y - ik_x}{k}\right)\Delta \\ \Delta_{++}(\vec{k}) &= f_p(k)\left(\tfrac{k_y + ik_x}{k}\right)\Delta. \end{aligned} \tag{1.11}$$

One can see that the proximity effect generates interband s-wave pairing encoded in the first term as well as intraband $p_x \pm ip_y$ pairing with opposite chirality for the upper/lower bands. As in the one-dimensional case, considering Δ much smaller than the inter-band distance, the upper band can be ignored. In this case, the problem maps onto that of spinless fermions with $p_x + ip_y$ pairing, which is the most basic example of a topological SC supporting a single Majorana bound state at a vortex core [21, 22]. Since the presence of a Majorana fermion has a topological origin, it cannot disappear as long as the bulk excitation gap remains finite. Ref. [8] studies the unprojected Hamiltonian and shows the gap closes for:

$$\mu_{\text{C}}^2 = V_{\text{Z}}^2 - \Delta^2. \tag{1.12}$$

Thus, for $\mu^2 < \mu_{\text{C}}^2$ the system is in the topological phase and for $\mu^2 > \mu_{\text{C}}^2$ it is in the trivial one.

1.4 Gapless Topological Superconducting Phase

Another relevant two-dimensional phase is the gapless topological SC phase [24]. This intrinsic gapless SC phase, hosts well localized edge states that coexist with a gapless bulk. The proposed realization for this phase involves a 2DEG with Rashba SOC, with a Hamiltonian similar to the one in Eq. (1.5) and proximity coupled to an s-wave SC. The twist in this case, comes in the form of a modulated magnetization term which instead of the Zeeman term reads: :

$$H_m = \int d^2r \psi_s^\dagger(\vec{r})\left(m\sigma_z \cos(Qx)\right)\psi_{s'}(\vec{r}) \tag{1.13}$$

with $Q = 2k_{\text{F}}$, where k_{F} is the Fermi momentum of the outer Fermi surface. For weak superconductivity, i.e. $|\Delta| < |m|$, it can be shown that one part of the Fermi surface is gapped by the magnetization and the other part is gapped by superconductivity [24]. Therefore, the nature of the gap changes along a path in momentum space and the gap is closed at the point of change. The band structure for $|\Delta| < |m|$ with open boundary conditions in the $\hat{x}$ direction is shown in Fig. 1.3. Two distinct gapless Dirac nodes are visible, as well as edge modes localized at the boundaries. These localized edge states indeed coexist with a gapless bulk, however they are protected by conservation of energy and momentum. Practically, For clean enough systems these edge states exhibit quantized thermal conductance and cause an enhanced local tunneling density of states (LDOS) near the edges, even when the LDOS at the bulk is non-zero.

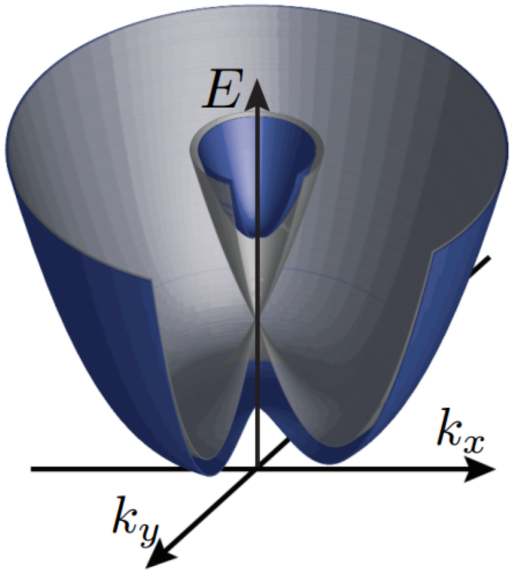

Figure 1.2: Spectrum of the Hamiltonian in Eq. (1.5). The gray surface represents the band structure of the Rashba SOC band in the absence of a time reversal breaking Zeeman field, while the blue surface represents the spectrum in the presence of such a field [23]. A low momentum massful Dirac cone emerges when the Zeeman field is applied in the $\hat{z}$ direction.

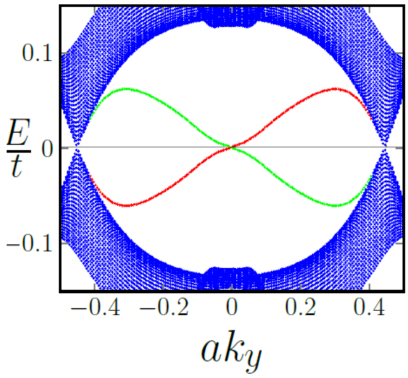

(a)

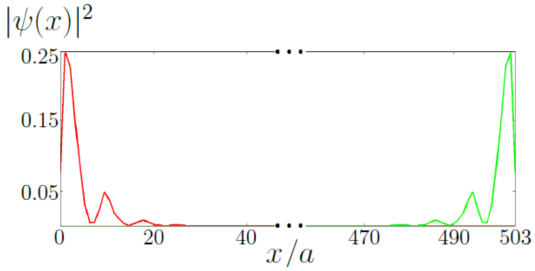

(b)

Figure 1.3: Topological SC phase characteristic signatures. (a) Band structure of the Hamiltonian from Eq. (1.5) with open boundary conditions in the $\hat{x}$ direction, coupled to an s-wave SC and subjected to a modulated magnetization [24]. a is the lattice spacing and t is the hopping term of the tight binding model used in Ref. [24]. The bulk spectrum is gapless at all energies, however the edge modes are clearly separated and are protected due to momentum and energy conservation. (b) Edge state wave functions that appear along the the $\hat{y}$ direction.

1.5 Gating in the Presence of a Superconductor

Naturally, proposed realization schemes for all of the topological SC phases presented above include conventional SCs, placed in proximity to various non-SC systems. In addition, in most proposals to realize such phases, the chemical potential of the system must reside in a specific and limited domain in order to facilitate the topological phase. These two requirements pose a great experimental challenge, as they effectively counter one another. When the system is in the presence of a SC that is close enough to enable the desired proximity effect, controlling its chemical potential with a gate is usually difficult due to screening by the SC, that can effectively weaken and even eliminate the effect of the external potential. In commonly used materials, there is a work function difference between the SCs and semiconductors, that implies that proximity between these materials causes transfer of electrons into the semiconductor. This is the cause for the often measured increase in the chemical potential of the semiconductor, as measured from the bottom of the conduction band, when placed in proximity to a SC.

In one-dimensional systems, the gating challenge was addressed by partially covering the nano-wire with the SC, which enabled some control of the electron density under the SC contact [11]. Recently, another approach was employed, of growing the SC as an island on the semiconductor [25], improving the ability to control the chemical potential via gate voltage due to the fact the SC is floating rather than grounded. Finite size floating SC islands may lead to a set of phenomena related to the charging energy of small systems. In this Thesis, we assume that the effective coupling between the SC islands is strong enough so the the charging effects can be neglected.

None of the above described two-dimensional SC phases have been experimentally observed. Currently, experimental efforts are focused on creating SC contacts to 2DEGs that enable good coupling, and possess diminished electron flooding properties. The ability to perform successful gating and to constrain the chemical potential to the domain required for the topological phase, is yet to be demonstrated in two-dimensional systems.

In this work, we propose addressing the challenge of gating by employing a SC-lattice geometry. In a SC lattice, the SC is deposited periodically on the sample, as is depicted in Fig. 3.1. In this apparatus, the electrostatic screening caused by the SC occurs only in certain spatial positions. In other spatial positions, which are not in proximity with the SC, the chemical potential is more easily controllable by the gate. Previous works proposed lattices of alternating chemical potential [26] and one-dimensional periodic structures of alternating SCs and gates [27, 28, 29, 30] as realizations of topological SCs.

Chapter 2

Goals and Thesis Outline

In this work, we introduce a SC lattice in which the SC is deposited periodically on a one or two-dimensional sample. We demonstrate that a SC lattice is a practical realization platform for a variety of topological SC phases, which overcomes the challenge of controlling the chemical potential of a system that is proximity coupled to a SC.

We begin in section 3, by describing the methods we use in order to obtain our results. In section 4.1, we show that zero-energy Majorana modes emerge at the ends of a one-dimensional system proximity coupled to a SC lattice. We analyze different regimes of the ratio between the SC lattice unit cell size and the Fermi wavelength of the system, and demonstrate that choosing them to be of the same order provides an optimal accessibility to the topological regions, while maximizing the gap which protects the Majorana bound states. Furthermore, we show results for a scenario in which the SOC exists only in the regions covered by a SC, which can resemble the case of a one-dimensional system composed of light chemical elements, such as a Carbon nanotube which has no substantial SOC, covered by a SC lattice composed of a heavy SC such as NbN.

In section 4.2.1, we show that zero-energy Majorana modes appear at the edges of a two-dimensional system proximity coupled to a SC lattice. Here too, we discuss a relatively practical case in which the SC lattice unit cell dimensions are of the order of the Fermi wavelength. We show that while the gap of the system is somewhat diminished, compared with the case of a uniform SC, the SC lattice platform allows to tune into the topological phase by controlling the potential only in the normal non-SC regions.

In addition, in section 4.2.2, we propose a relatively simple realization scheme for the gapless topological SC phase, that involves a 2DEG with strong SOC proximity coupled to an s-wave SC, in the presence of *in-plane* magnetization. The last feature allows the topological SC phase to be experimentally accessed using in plane magnetic field, that does not entail orbital effects. We show that proximity coupling the SC in a super-lattice geometry to this system, rendering the chemical potential requirement experimentally achievable, provides well localized edge modes coexisting with a gapless bulk.

In particular, we demonstrate that even when assuming the worst case of absolute screening, in which the chemical potential under the SC is completely unaffected by the external gate potential, all of the above described topological SC phases can be reached. We study how varying experimentally controllable parameters such as the magnetic field, the chemical potential in the normal regions and the lengths of the SC and normal regions, allows to tune into these topological SC phases. Moreover, we establish that these phases are sustained over finite and substantial regions in the space of tunable parameters, exemplifying the known robustness of topological phases. We attempt to address some experimental considerations and to provide prescriptions regarding length scales, materials and geometries to be used.

In chapter 5, we present experimentally accessible signatures of these topological SC phases, and propose a realizable Majorana braiding procedure that utilizes the periodic nature of our SC lattice scheme. Finally, in chapter 6 we conclude.

Chapter 3

Methods

3.1 Analytical Model

3.1.1 One-Dimensional Superconducting Lattice

In order to address the gating issue, we consider a scenario in which the SC is periodically deposited in a super-lattice geometry on a one-dimensional system, as depicted in Fig. 3.1a. We analyze a one-dimensional wire with Rashba SOC, placed in an external magnetic field and covered by a SC lattice. The Hamiltonian of the system is given by:

$$\begin{aligned} H = \int dx \psi_s^\dagger(x) \left[-\tfrac{\nabla^2}{2m} - \mu(x) + i\alpha\partial_x\sigma_y + V_Z\sigma_x \right] \psi_{s'}(x) \\ + \Big(\Delta(x)\, \psi_\uparrow^\dagger(x) \psi_\downarrow^\dagger(x) + \text{H.c.} \Big), \end{aligned} \tag{3.1}$$

where m is the effective electron mass, α is the Rashba SOC constant, V_Z is the Zeeman coupling due to the applied magnetic field, $\mu(x)$ is the spatially dependant chemical potential and $\Delta(x)$ is the spatially dependant induced pairing potential as a result of the superconducting proximity effect. σ_j are Pauli matrices that act on the spin degree of freedom of ψ. For uniform $\mu(x) = \mu_0$ and $\Delta(x) = \Delta_0$, this Hamiltonian resembles the Hamiltonian in Eq. (1.1), which was shown to be in the topological phase for: $|\mu_0| < \sqrt{V_Z^2 - \Delta_0^2} \equiv \mu_C$.

In actual experimental setups, the chemical potential of a semiconducting wire coupled to an s-wave SC is typically much higher than μ_C, due to the work function difference between the SC and the wire. In the absence of control over the chemical potential (for instance, due to screening), the system will remain trivial.

We model the SC lattice in Fig. 3.1a by choosing the spatial profile of the pairing potential $\Delta(x) = \Delta_0 \cdot f(x)$ to be:

$$\begin{gathered} f(x) = \textstyle\sum_j \text{rect}\left(\frac{x}{L_S} - j \cdot L \right) = \sum_n f_{G_n} e^{ixG_n} \\ f_{G_n} = \tfrac{L_S}{L} \text{sinc}\left(\tfrac{G_n \cdot L_S}{2\pi} \right), \end{gathered} \tag{3.2}$$

where L and L_S are the lengths of the super-lattice unit cell and the SC segment inside each unit cell, respectively. $G_n = \frac{2\pi n}{L}$, $n \in \mathbb{Z}$ is a general inverse lattice vector for the super-lattice, and f_{G_n} is its corresponding Fourier component. The functions $\text{rect}(x)$ and $\text{sinc}(x)$ are given by:

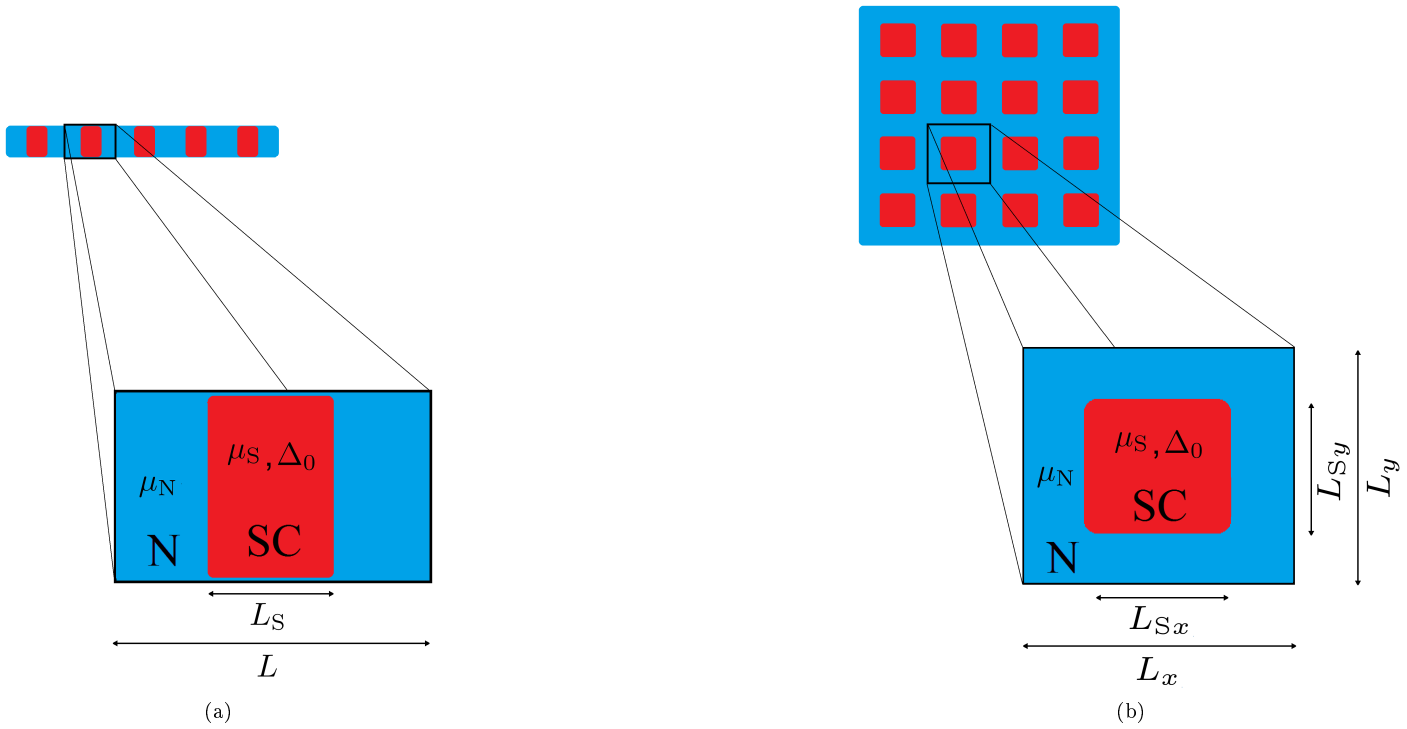

Figure 3.1: A schematic illustration of a system covered by a SC lattice in (a) one dimension and (b) two dimensions. Under each system is an enlarged picture of a unit cell of which the super-lattice is composed, where lengths and quantities are marked. Red color marks regions with induced SC due to contact with a SC, while blue marks normal regions not in proximity to a SC. The red regions have an induced pairing of Δ_0 and a chemical potential μ_{S}. The blue regions have no induced pairing term, and a chemical potential μ_{N}. The chemical potential values to be used for μ_{S} and μ_{N} are given by the distance between the bottom of the conduction band in the respective regions to the general electro-chemical potential, which is uniform in equilibrium.

$$\begin{gathered}\mathrm{rect}(x)=\begin{cases}0 & \text{for} \quad |x|>0.5\\ 0.5 & \text{for} \quad |x|=0.5\\ 1 & \text{for} \quad |x|<0.5\end{cases}\\ \mathrm{sinc}(x)=\frac{\sin(\pi x)}{\pi x}\ .\end{gathered} \tag{3.3}$$

We would like to assume nothing regarding the ability to control the chemical potential in the regions covered by a SC, which we denote as μ_{S}. Specifically, we model a scenario where μ_{S} is unaffected by an attempt of gating it due to screening by the SC. On the other hand, we assume that the chemical potential in the normal regions not covered by a SC, which we denote as μ_{N}, can be controlled by an external gate, as they are not in proximity to a SC.

Overall, we analyze a spatial distribution for the chemical potential of the same form as the pairing potential distribution: $\mu(x)=\mu_{\mathrm{S}}\cdot f(x)$. We choose $\mu_{\mathrm{S}}>\mu_{\mathrm{C}}$, and the form of $f(x)$ dictates $\mu_{\mathrm{N}}=0$ which obviously upholds the required condition for the topological phase given in Eq. (1.4). It is noteworthy, that the chemical potential values to be used for μ_{S} and μ_{N} are the distance between the bottom of the conduction band in the respective regions to the general electro-chemical potential, which is uniform in equilibrium.

Let $r=L_{\mathrm{S}}/L<1$ be the fraction of the unit cell covered by a SC. Bellow, we will compare the modulation period of the SC lattice to a characteristic Fermi wavelength. For an estimation of this wavelength, we diagonalize the Hamiltonian in Eq. (3.1) for $\Delta(x)=0$ and a constant average value of the chemical potential $\bar{\mu}=r\mu_{\mathrm{S}}+(1-r)\mu_{\mathrm{N}}$. The Fermi momentum and wavelength of the outer band are:

$$\begin{gathered}k_{\mathrm{F}}=\sqrt{2m^2\alpha^2+2m\bar{\mu}+2m\sqrt{V_{\mathrm{Z}}^2+m^2\alpha^4+2m\alpha^2\bar{\mu}}}\\ \lambda_{\mathrm{F}}=\tfrac{2\pi}{k_{\mathrm{F}}}.\end{gathered} \tag{3.4}$$

In the presence of these periodic potentials, the Hamiltonian of the system written in momentum space is:

$$\begin{aligned}H=\int_{-\frac{\pi}{L}}^{\frac{\pi}{L}}dk\sum_n\Big\{&\psi^\dagger_{sk-G_n}\left[\tfrac{(k-G_n)^2}{2m}-\alpha(k-G_n)\sigma_y+V_{\mathrm{Z}}\sigma_z\right]\psi_{s'k-G_n}\\ &+\Delta_0 f_{G_n}\psi^\dagger_{\uparrow k}\psi^\dagger_{\downarrow G_n-k}+\mu_{\mathrm{S}}f_{G_n}\psi^\dagger_{sk}\psi^\dagger_{\downarrow k-G_n}+\mathrm{H.c.}\quad\Big\}.\end{aligned} \tag{3.5}$$

We keep only the zeroth and first harmonics of the periodic potential, which essentially means we approximate it to be a cosine plus a constant potential in real space. Thus, we neglect any matrix elements that correspond to momenta of G_2 and higher. The topological properties of the system are weakly affected by this approximation for $L\ll\lambda_{\mathrm{F}}$ [31], since the neglected matrix elements alter the spectrum at high energies. For $L\sim\lambda_{\mathrm{F}}$, we will use a tight-binding approximation (see section 3.2) rather than the formulas derived below. Defining the Nambu spinor $\Psi_k=\begin{pmatrix}\psi_{k\uparrow}, & \psi_{k\downarrow}, & \psi^\dagger_{-k\downarrow}, & -\psi^\dagger_{-k\uparrow}\end{pmatrix}^T$, we make an approximation valid for $L\ll\lambda_{\mathrm{F}}$ where only the bands at G_n with $n=0,\pm1$ are kept and the Hamiltonian becomes :

$$\begin{aligned}H&=\tfrac{1}{2}\int_{-\frac{\pi}{L}}^{\frac{\pi}{L}}dk\begin{pmatrix}\Psi^\dagger_{k+G_{-1}} & \Psi^\dagger_k & \Psi^\dagger_{k+G_1}\end{pmatrix}H(k)\begin{pmatrix}\Psi_{k+G_{-1}}\\ \Psi_k\\ \Psi_{k+G_1}\end{pmatrix}\\ H(k)&=\begin{pmatrix}h_0(k+G_{-1}) & h_1 & 0\\ h_{-1} & h_0(k) & h_1\\ 0 & h_{-1} & h_0(k+G_1)\end{pmatrix},\end{aligned} \tag{3.6}$$

where the uniform and the first harmonic terms are:

$$\begin{aligned} h_0(k) &= \left(\tfrac{k^2}{2m} - f_{G_0}\mu_{\mathrm{S}} - \alpha k\sigma_y\right)\tau_z + V_{\mathrm{Z}}\sigma_z + f_{G_0}\Delta_0\tau_x \\ h_{\pm 1} &= f_{G_{\pm 1}}\Delta_0\tau_x - f_{G_{\pm 1}}\mu_{\mathrm{S}}\tau_z, \end{aligned} \tag{3.7}$$

with τ_j the Pauli matrices that act on the particle-hole degree of freedom. Overall $H(k)$ is in this case a 12×12 matrix, in the space of spin, particle hole and inverse lattice vectors degrees of freedom. The zeros in $H(k)$ originate in the approximation of the potential to a cosine potential in real space. The fact that it is only of size 3×3 in the inverse lattice space is due to keeping only the first momentum space replicas [32]. It is noteworthy, that the zeroth Fourier component f_{G_0}, appearing in $h_0(k)$, is equal to the average of the distribution $f(x)$. This means that in effect, for any amount of harmonic terms kept in the periodic potential, $f_{G_0}\mu_{\mathrm{S}} = r\mu_{\mathrm{S}}$ and $f_{G_0}\Delta_0 = r\Delta_0$.

In order to investigate the topological properties of this Hamiltonian, we note its symmetries. It obeys a time reversal symmetry given by $\mathcal{T} = \kappa$, where κ stands for complex conjugation. The Hamiltonian upholds:

$$\mathcal{P}H(k)\mathcal{P}^{-1} = -H(-k), \tag{3.8}$$

where $\mathcal{P}$ is the particle-hole operator given by $\mathcal{P} = \Lambda\kappa$, and Λ is given by:

$$\Lambda = \begin{pmatrix} 0 & 0 & 1 \\ 0 & 1 & 0 \\ 1 & 0 & 0 \end{pmatrix} \otimes i\tau_y \otimes \sigma_y. \tag{3.9}$$

$\mathcal{P}$ and $\mathcal{T}$ square to the value of $+1$, therefore the system is in class BDI of the topological classification given in [33], and is characterized by a $\mathbb{Z}$ topological invariant [34, 35]. We are only interested in the parity of this $\mathbb{Z}$ topological invariant [36], which has been shown by Ref. [37] to be equivalent to the $\mathbb{Z}_2$ topological invariant of class D given by [5, 38]:

$$P = \mathrm{sgn}\left\{\mathrm{Pf}\left[\Lambda H(k=0)\right]\right\} \cdot \mathrm{sgn}\left\{\mathrm{Pf}\left[\Lambda H(k=\frac{\pi}{L})\right]\right\}. \tag{3.10}$$

3.1.2 Two-Dimensional Superconducting Lattice

For the realization of the two-dimensional topological SC phases, we consider a 2DEG with Rashba SOC, in the presence of a Zeeman field, covered by a SC lattice, as depicted in Fig. 3.1b. The Hamiltonian describing the system is given by:

$$\begin{aligned} H = \int d^2r \psi_s^\dagger(\vec{r}) \left[-\tfrac{\nabla^2}{2m} - \mu(\vec{r}) - i\alpha\left(\partial_y\sigma_x - \partial_x\sigma_y\right) + V_{\mathrm{Z}}\hat{\mathbf{d}}\cdot\boldsymbol{\sigma}\right]\psi_{s'}(\vec{r}) \\ + \Big(\Delta(\vec{r})\,\psi_\uparrow^\dagger(\vec{r})\psi_\downarrow^\dagger(\vec{r}) + \mathrm{H.c.}\Big), \end{aligned} \tag{3.11}$$

where m, α, V_{Z}, μ, and Δ represent the same quantities as in the one-dimensional case. Below we consider separately the case of $\hat{\mathbf{d}} = \hat{z}$ (perpendicular) and $\hat{\mathbf{d}} = \hat{y}$ (in plane). The two cases give rise to a $p_x + ip_y$ topological SC phase and a gapless topological SC phase, respectively.

3.1.2.1 Topological $p_x + ip_y$ Superconducting Phase

We first discuss the realization of the $p_x + ip_y$ topological SC phase, where the magnetization term in the $\hat{d} = \hat{z}$ direction. In our analysis we disregard orbital magnetic effects that would be present when applying a perpendicular magnetic field. A Zeeman term without such effects can be achieved by proximity coupling the system to a ferromagnet. Alternatively,

the $p_x + ip_y$ phase can be realized with an in-plane magnetic field in a system with strong Dresselhous SOC (such as a 110-grown InSb quantum well) [20]. For simplicity, and since the emphasis of this thesis is the use of a SC lattice to address the gating issue, we focus solely on a Zeeman term in the perpendicular direction. For further discussion of experimental considerations, see section 5.2.1.

For uniform $\mu(\vec{r}) = \mu_0$ and $\Delta(\vec{r}) = \Delta_0$, the Hamiltonian in Eq. (3.11) resembles the system analyzed in Section 1.3, that has been shown to be driven into the topological $p_x + ip_y$ SC phase for $|\mu_0| < \sqrt{V_Z^2 - \Delta_0^2} \equiv \mu_C$ [8]. We model the SC lattice in Fig. 3.1b. by choosing the spatial profile of the pairing potential $\Delta(\vec{r}) = \Delta_0 \cdot f(\vec{r})$ as:

$$\begin{gathered} f(\vec{r}) = \sum_{j,l} \mathrm{rect}\left(\frac{x}{L_{Sx}} - j \cdot L_x\right) \cdot \mathrm{rect}\left(\frac{y}{L_{Sy}} - l \cdot L_y\right) = \sum_{n,m} f_{\vec{G}_{n,m}} e^{i\vec{r}\cdot\vec{G}_{n,m}} \\ f_{\vec{G}_{n,m}} = \frac{L_{Sx}\cdot L_{Sy}}{L_x \cdot L_y} \cdot \mathrm{sinc}\left(\frac{(\vec{G}_{n,m})_x L_{Sx}}{2\pi}\right) \cdot \mathrm{sinc}\left(\frac{(\vec{G}_{n,m})_y L_{Sy}}{2\pi}\right), \end{gathered} \tag{3.12}$$

where L_x, L_y are the lengths of the super-lattice unit cell and L_{Sx}, L_{Sy} are the lengths of the SC segment inside each unit cell in the $\hat{x}$ and $\hat{y}$ directions, respectively. $\vec{G}_{n,m} = \left(\frac{2\pi}{L_x}n, \frac{2\pi}{L_y}m\right)$, $n, m \in \mathbb{Z}$ is a general inverse lattice vector for the super-lattice and $f_{\vec{G}_{n,m}}$ is its corresponding Fourier component. As in the one-dimensional case, we will analyze a spatial distribution for the chemical potential of the same form as the pairing potential distribution: $\mu(\vec{r}) = \mu_0 \cdot f(\vec{r})$, where we choose $|\mu_0| > |\mu_C|$, resulting in $|\mu_S| > |\mu_C|$ and $\mu_N = 0$.

In the presence of these periodic potentials, the Hamiltonian of the system written in momentum space is:

$$\begin{gathered} H = \int_{-\frac{\pi}{L_x}}^{\frac{\pi}{L_x}} dk_x \int_{-\frac{\pi}{L_y}}^{\frac{\pi}{L_y}} dk_y \Big\{ \sum_{n,m} \psi^\dagger_{s\vec{k}-\vec{G}_{n,m}} \Big[\tfrac{(k_x-(\vec{G}_{n,m})_x)^2+(k_y-(\vec{G}_{n,m})_y)^2}{2m} + \\ \alpha\left((k_y-(\vec{G}_{n,m})_y)\sigma_x - (k_x-(\vec{G}_{n,m})_x)\sigma_y\right) + V_Z\sigma_z \Big] \psi_{s'\vec{k}-\vec{G}_{n,m}} \\ +\Delta_0 f_{\vec{G}_{n,m}} \psi^\dagger_{\uparrow\vec{k}} \psi^\dagger_{\downarrow\,\vec{G}_{n,m}-\vec{k}} + H.c. \\ +\mu_0 f_{\vec{G}_{n,m}} \psi^\dagger_{s\vec{k}} \psi^\dagger_{s\,\vec{k}-\vec{G}_{n,m}} + H.c. \Big\}. \end{gathered} \tag{3.13}$$

As in the one-dimensional case, we keep only the zeroth and first harmonics of the periodic potential, neglecting any matrix elements that correspond to momentum transfer of over $\max(\frac{2\pi}{L_x}, \frac{2\pi}{L_y})$. Defining the Nambu spinor

$\Psi_{\vec{k}} = \begin{pmatrix} \psi_{\vec{k}\uparrow}, & \psi_{\vec{k}\downarrow}, & \psi^\dagger_{-\vec{k}\downarrow}, & -\psi^\dagger_{-\vec{k}\uparrow} \end{pmatrix}^T$, we keep only the bands at $\vec{G}_{n,m}$ with $n, m = 0, \pm 1$ and the Hamiltonian becomes:

$$H = \tfrac{1}{2}\int_{-\frac{\pi}{L_x}}^{\frac{\pi}{L_x}} dk_x \int_{-\frac{\pi}{L_y}}^{\frac{\pi}{L_y}} dk_y \begin{pmatrix} \Psi^\dagger_{\vec{k}+\vec{G}_{0,-1}} & \Psi^\dagger_{\vec{k}+\vec{G}_{-1,0}} & \Psi^\dagger_{\vec{k}} & \Psi^\dagger_{\vec{k}+\vec{G}_{1,0}} & \Psi^\dagger_{\vec{k}+\vec{G}_{0,1}} \end{pmatrix} H_{\vec{k}} \begin{pmatrix} \Psi_{\vec{k}+\vec{G}_{0,-1}} \\ \Psi_{\vec{k}+\vec{G}_{-1,0}} \\ \Psi_{\vec{k}} \\ \Psi_{\vec{k}+\vec{G}_{1,0}} \\ \Psi_{\vec{k}+\vec{G}_{0,1}} \end{pmatrix}$$

$$H_{\vec{k}} = \begin{pmatrix} h_0\left(\vec{k}+\vec{G}_{0,-1}\right) & 0 & h_1^y & 0 & 0 \\ 0 & h_0\left(\vec{k}+\vec{G}_{-1,0}\right) & h_1^x & 0 & 0 \\ h_{-1}^y & h_{-1}^x & h_0\left(\vec{k}\right) & h_1^x & h_1^y \\ 0 & 0 & h_{-1}^x & h_0\left(\vec{k}+\vec{G}_{1,0}\right) & 0 \\ 0 & 0 & h_{-1}^y & 0 & h_0\left(\vec{k}+\vec{G}_{0,1}\right) \end{pmatrix}, \tag{3.14}$$

where the uniform and the first harmonic terms are:

$$\begin{aligned} h_0(\vec{k}) &= \left(\tfrac{k^2}{2m} - f_{\vec{G}_{0,0}} \cdot \mu_0 - \alpha(k_x\sigma_y - k_y\sigma_x)\right)\tau_z + V_Z\sigma_z \\ &\quad + f_{\vec{G}_{0,0}} \cdot \Delta_0\tau_x \\ h^x_{\pm 1} &= f_{\vec{G}_{\pm 1,0}} \cdot \Delta_0\tau_x - f_{\vec{G}_{\pm 1,0}} \cdot \mu_0\tau_z \\ h^y_{\pm 1} &= f_{\vec{G}_{0,\pm 1}} \cdot \Delta_0\tau_x - f_{\vec{G}_{0,\pm 1}} \cdot \mu_0\tau_z. \end{aligned} \tag{3.15}$$

The Hamiltonian upholds $\mathcal{P}H_{\vec{k}}\mathcal{P}^{-1} = -H_{-\vec{k}}$, with the particle-hole operator:

$$\mathcal{P} = \begin{pmatrix} 0 & 0 & 0 & 0 & 1 \\ 0 & 0 & 0 & 1 & 0 \\ 0 & 0 & 1 & 0 & 0 \\ 0 & 1 & 0 & 0 & 0 \\ 1 & 0 & 0 & 0 & 0 \end{pmatrix} \otimes i\tau_y \otimes \sigma_y\kappa, \tag{3.16}$$

which squares to $+1$. It does not obey time reversal symmetry, so it is in class D of the topological classification given in Ref. [33]. In two dimensions, this implies a $\mathbb{Z}$ invariant [34, 35] given by the Chern number:

$$\nu = \frac{1}{\pi}\sum_n \int_{-\frac{\pi}{L_x}}^{\frac{\pi}{L_x}} dk_x \int_{-\frac{\pi}{L_y}}^{\frac{\pi}{L_y}} dk_y \mathrm{Im}\left\langle \partial_{k_x}\varphi_n | \partial_{k_y}\varphi_n \right\rangle, \tag{3.17}$$

where φ_n are the eigenstates of the Hamiltonian in Eq. (3.14), and the sum runs over the negative energy bands. From computational efficiency considerations, we follow Ref. [39] for calculating the parity of the Chern number as the sum of weak indices. We verify the actual value of the Chern number by calculating the integral in Eq. (3.17) for a representative point within each gapped region in the parameter space.

3.1.2.2 Gapless Topological Superconducting Phase

We will analyze the Hamiltonian in Eq. (3.11), with in plane magnetic field in the direction $\hat{d} = \hat{y}$. In order to look for a signature for the gapless topological SC phase, we will analyze a system with open boundary conditions in the $\hat{y}$ direction. Gapless states localized at the edges of the system, clearly separated in momentum or energy from the bulk states, will be the hallmark of this phase. An experimentally accessible signature for this phase, will be an enhanced LDOS near the edges of the system.

The LDOS is by definition given by a sum of delta functions at the eigen-energies E_m of the Hamiltonian, weighted by their corrisponding eigen-functions:

$$\mathcal{N}(\vec{r}, E) = \sum_m |\phi_m(\vec{r})|^2 \delta\left(E - E_m\right)$$

We define the retarded green's function:

$$G(\vec{r}, \vec{r}', E) = \lim_{\eta\to 0^+} \langle\vec{r}| \left[E - H + i\eta\right]^{-1} |\vec{r'}\rangle = \lim_{\eta\to 0^+} \sum_{mm'} \langle\vec{r}|m\rangle\langle m| \left[E - H + i\eta\right]^{-1} |m'\rangle\langle m'|\vec{r}\rangle = \lim_{\eta\to 0^+} \sum_m \frac{\phi^*_m(\vec{r})\phi_m(\vec{r}')}{E - E_m + i\eta}. \tag{3.18}$$

Using the relation $\delta(x) = -\frac{1}{\pi}\mathrm{Im}\left[\lim_{\eta\to 0^+}\frac{1}{x+i\eta}\right]$ we find that the local density of states is give by:

$$\mathcal{N}(\vec{r},E) = -\frac{1}{\pi}\mathrm{Im}[G(\vec{r},\vec{r},E)]. \tag{3.19}$$

The LDOS will be used to demonstrate the emergence of edge states in all of the topological phases.

3.2 Tight-Binding Model for Simulations

3.2.1 The Model

The tight-binding model will allow us to numerically evaluate the topological invariants, as well as the LDOS of the zero energy excitations, for a general form of the spatial distribution of the SC lattice. In this section we present the method of finite differences as a technique to discretize the Hamiltonian of a continuous system. This is obtained by discretizing the Hamiltonian on a lattice, where the lattice spacing is chosen such that it is smaller than the relevant physical parameters of the system, as the Fermi wavelength, the SOC length etc. The lattice sites themselves do not in general correspond to an atom, but describe a region of the system in a coarse graining sense. It is noteworthy, that the tight-binding lattice sites are not directly related to the above discussed super-lattice model this work presents.

3.2.2 One-Dimensional Tight-Binding

The scheme for discretizing the one-dimensional real space Hamiltonian given in Eq. (3.1) is as follows. A lattice with a lattice parameter a is introduced, which defines the lattice points $x = na$, $n = 1, ..., N$. N is the number of sites, and Na represents the physical length of the entire system. The lattice creation operators are related to the operators of the continuous case by:

$$\psi_s^\dagger(x = na) \to \frac{1}{\sqrt{a}}c_{ns}^\dagger. \tag{3.20}$$

The derivative operators are then approximated by the method of finite differences:

$$\begin{array}{c}\partial_x f(x) \to \frac{1}{2a}\left[f(x+a) - f(x-a)\right] \\ \partial_x^2 f(x) \to \frac{1}{a^2}\left[f(x+a) - 2f(x) + f(x-a)\right].\end{array} \tag{3.21}$$

Converting all integrals into sums $\int dx \to \sum_{\substack{x=na \\ n=1,\ldots,N}}$, the Hamiltonian in Eq. (3.1), with the spatial profile of Δ and μ as given in Eq. (3.2), is mapped to:

$$\begin{array}{c} H_{tb} = \sum_{n,s,s'} c_{n;s}^\dagger \epsilon_{n;ss'} c_{n,s'} + \left[c_{n;s}^\dagger t_{ss'} c_{n+1,s'} + h.c.\right] + \sum_n \left[\Delta_n c_{n;\uparrow}^\dagger c_{n;\downarrow}^\dagger + h.c.\right] \\ \epsilon_{n;ss'} = (2t - \mu_n)\,\delta_{ss'} + V_Z \sigma_{ss'}^z \\ t_{ss'} = -t\delta_{ss'} - iu\sigma_{ss'}^y \\ \mu_n = \mu_0 f_n \\ \Delta_n = \Delta_0 f_n \\ f_n = \sum_j \mathrm{rect}\left(\frac{na}{Ls} - j\cdot L\right), \end{array} \tag{3.22}$$

where $t = 1/2ma^2$ and $u = \alpha/2a$. $t_{ss'}$ represents the hopping amplitude between the sites of the wire, with the $-t\delta_{ss'}$ term originating in the kinetic term, and $-iu\sigma^y_{ss'}$ originating in the Rashba SOC term. Notice that the periodic nature is preserved, where each unit cell is now composed of L/a sites of which L_S/a are in proximity to a SC (we assume L and L_S are integer multiples of a).

In order to model real experimental systems using tight-binding Hamiltonians, we can relate the tight-binding parameters t, u to the physical parameters used in experiments. The SOC energy and length are given by:

$$\begin{aligned} E_{\mathrm{SO}} &= \tfrac{u^2}{t} \\ l_{\mathrm{SO}} &= a\tfrac{t}{u}. \end{aligned} \tag{3.23}$$

Given physical values for E_{SO}, L and m, and specifying a number of unit cells, we can compute all the tight-binding parameters. In order for the tight-binding model to accurately describe its continuous counterpart, we require the bandwidth $4t$ to be larger than all other energy scales in the system: $4t \gg E_{\mathrm{SO}}$, Δ, V, μ_0.

The Fermi wavelength in terms of the tight-binding parameter a, is calculated similarly to Eq. (3.4), and is given by:

$$\begin{aligned} k_{\mathrm{F}} &= \sqrt{2\tfrac{u^2}{t^2} + \tfrac{\bar{\mu}}{t} + \tfrac{2}{t^2}\sqrt{\tfrac{t^2V_{\mathrm{Z}}^2}{4} + u^2 + tu^2\bar{\mu}}} \\ \lambda_{\mathrm{F}} &= \tfrac{2\pi}{k_{\mathrm{F}}}. \end{aligned} \tag{3.24}$$

3.2.3 Two-Dimensional Tight-Binding

The extension of the tight-binding procedure to two dimensions is simple. a_x and a_y define the lattice points $x = na_x$ and $y = ma_y$. The indices n and m count the sites between 1 and N_x, N_y, in the $\hat{x}$ and $\hat{y}$ directions respectively. Thus, N_xa_x and N_ya_y represent the physical lengths of the system in these respective directions. The Hamiltonian in Eq. (3.11), with the spatial profile of Δ and μ as given in Eq. (3.12), is mapped to:

$$\begin{aligned} H_{tb} = \sum_{n,m,s,s'} c^\dagger_{n,m;s}\epsilon_{nm;ss'}c_{n,m;s'} + \left[c^\dagger_{n,m;s}t^x_{ss'}c_{n+1,m;s'} + h.c.\right] + \left[c^\dagger_{n,m;s}t^y_{ss'}c_{n,m+1;s'} + H.c.\right] + \sum_n \left[\Delta_{n,m}c^\dagger_{n,m;\uparrow}c^\dagger_{n,m;\downarrow} + H.c.\right] \\ \epsilon_{nm;ss'} = (2t - \mu_{nm})\,\delta_{ss'} + V_{\mathrm{Z}}\hat{\mathbf{d}}\cdot\boldsymbol{\sigma}_{ss'} \\ t^x_{ss'} = -t\delta_{ss'} - iu\sigma^y_{ss'} \\ t^y_{ss'} = -t\delta_{ss'} + iu\sigma^x_{ss'} \\ \mu_{nm} = \mu_0 f_{nm} \\ \Delta_{nm} = \Delta_0 f_{nm} \\ f_{nm} = \sum_{j,l}\mathrm{rect}\left(\tfrac{na_x}{L_{\mathrm{S}x}} - j\cdot L_x\right)\cdot\mathrm{rect}\left(\tfrac{ma_y}{L_{\mathrm{S}y}} - l\cdot L_y\right). \end{aligned} \tag{3.25}$$

3.2.4 Super-Lattice Momentum Space

We will utilize the periodic nature of the super-lattice potential for analyzing the topological properties of our tight-binding Hamiltonians. To do so, let us write a general tight-binding model for a periodic system:

$$H = \sum_{rr'jj'} c^\dagger_{r,j}h\left(r - r', j, j'\right)c_{r',j'}. \tag{3.26}$$

Where the r, r' indices represent the unit cell index and the j, j' indices represent the sites inside each unit cell including all of their degrees of freedom (site index, spin, particle-hole). The matrix element h depends only on the difference R=$r - r'$ due to the periodic nature of the super-lattice. The Hamiltonian in the space of momentum which corresponds to the super lattice unit cells can be written as:

$$\begin{aligned} H &= \sum_{k,j,j'} c^{\dagger}_{k,j} h_k\left(j,j'\right) c_{k,j'} \\ h_k\left(j,j'\right) &= \sum_{R=-\infty}^{\infty} e^{ikR} h\left(R,j,j'\right) \\ c^{\dagger}_{r,j} &= \sum_k c^{\dagger}_{k,j} e^{ikr}. \end{aligned} \tag{3.27}$$

For nearest neighbors hopping models such as the one presented above, $h\left(R,j,j'\right)$ is non-zero only for $R = 0, \pm 1$. The information describing the internal structure of the unit cell will reside in $h\left(0,j,j'\right)$, and the hopping between neighboring unit cells elements will be in $h\left(\pm 1,j,j'\right)$. If n^* is the amount of sites composing a unit cell, k runs between $-\pi/n^*a$ and π/n^*a, while the usual tight-binding momentum defined for uniform systems which runs between $-\pi/a$ and π/a. Thus, the tight-binding equivalent of the $\mathbb{Z}_2$ invariant given in Eq. (3.10) would be:

$$P = \operatorname{sgn}\left\{\operatorname{Pf}\left[\Lambda H(k=0)\right]\right\} \cdot \operatorname{sgn}\left\{\operatorname{Pf}\left[\Lambda H(k=\frac{\pi}{n^*a})\right]\right\}, \tag{3.28}$$

with $\mathcal{P} = \Lambda\kappa$ the particle-hole operator and Λ is given by:

$$\Lambda = 1_{sites} \otimes i\tau_y \otimes \sigma_y, \tag{3.29}$$

where 1_{sites} is the identity matrix in the space of tight-binding sites.

The extension of this super-lattice momentum space treatment to two dimensions is similar to the one-dimentional case shown in Eqs. (3.26) and (3.27), and it results in a two-dimensional momentum space Hamiltonian $h_{\vec{k}}$. If ψ_q are the eigenstates of $h_{\vec{k}}$, the $\mathbb{Z}$ topological invariant is given by Chern number:

$$\nu = \frac{1}{\pi}\sum_q \int_{-\frac{\pi}{L_x}}^{\frac{\pi}{L_x}} dk_x \int_{-\frac{\pi}{L_y}}^{\frac{\pi}{L_y}} dk_y \operatorname{Im}\left\langle \partial_{k_x}\psi_q | \partial_{k_y}\psi_q \right\rangle, \tag{3.30}$$

where the sum runs over the negative energy bands. An illustration of the super-lattice unit cell and momentum is presented in Fig. 3.2.

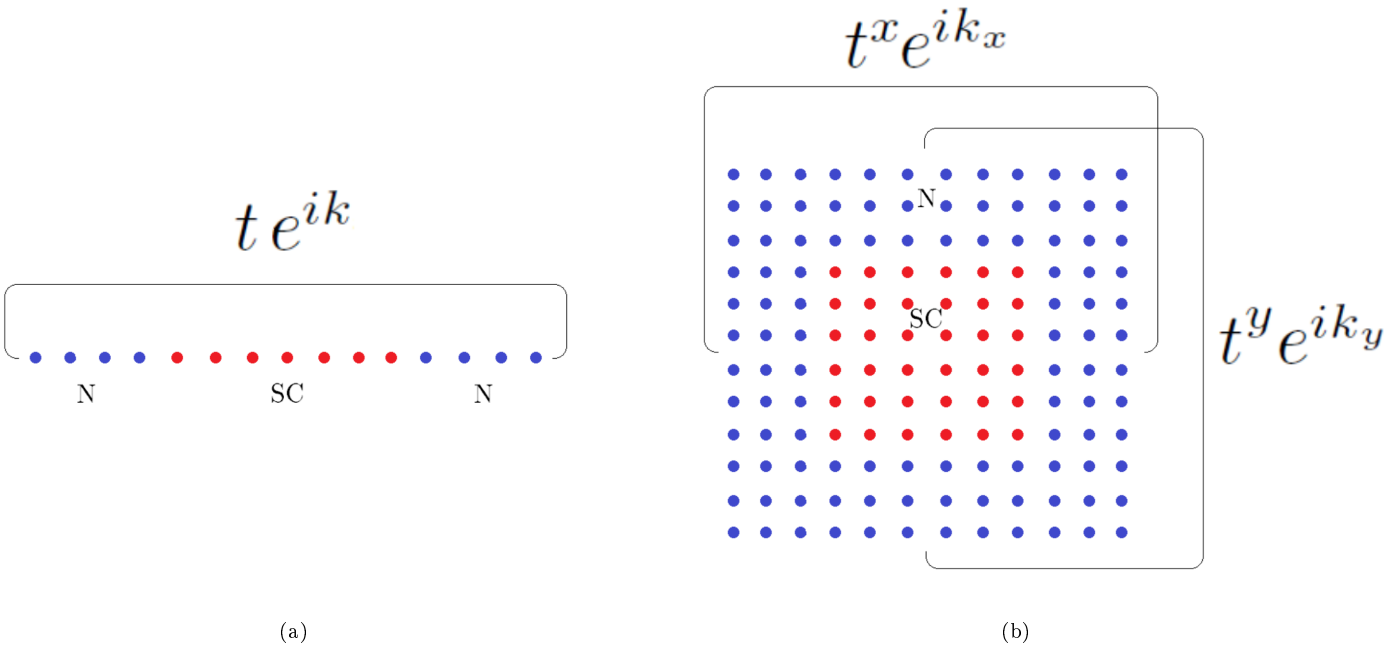

(a) (b)

Figure 3.2: An illustration of a tight-binding unit cell and the momenta corresponding to the super lattice periodicity. Red sites represent regions with induced SC due to contact with a SC, blue sites represent normal regions not in proximity to a SC. (a) A one-dimensional tight-binding model of the super-lattice unit cell. The additional hopping term between the first and last sites which rises from Eq. (3.27), represents the hopping between adjacent unit cells that receives a te^{ik} factor, where k is the super-lattice momentum. (b) A two-dimensional tight-binding model of the super-lattice unit cell. In this case, each site located on one of the edges has a hopping term to the opposite edge, which represents the hopping between adjacent unit cells and is multiplied by the corresponding $t^j e^{ik_j}$ factor. k_j is the super-lattice momentum in the direction j.

Chapter 4

Results

4.1 One-Dimensional Phase

4.1.1 Results for $L \ll \lambda_F$

We investigate the phase diagram of the system depicted in Fig. 3.1a in the limit where the unit cell is much shorter than the Fermi wavelength, $L \ll \lambda_{\mathrm{F}}$. In this limit, one expects that the electrons effectively experience the *average* values of $\mu(x)$ and $\Delta(x)$. A similar effect was concluded in Ref. [42] in the case of a SC-ferromagnetic super-lattice. Observing Eqs. (3.6) and (3.7), $L \ll \lambda_{\mathrm{F}}$ implies that $h_{\pm 1}$ can be disregarded. Recalling that $f_{G_0} = r$ (see Fourier component definition in Eq. (3.2)), we can indeed expect the effective values of the chemical and induced pairing potentials to be their spatial average:

$$\begin{aligned} \bar{\mu} &= r\mu_{\mathrm{S}} + (1-r)\mu_{\mathrm{N}} \\ \bar{\Delta} &= r\Delta_0. \end{aligned} \tag{4.1}$$

We begin the analysis by examining the case where μ_{N} is tuned to 0 by a gate potential. In this $L \ll \lambda_{\mathrm{F}}$ limit, we expect the phase transition to occur at [9, 10]:

$$r^2\left(\Delta_0^2 + \mu_{\mathrm{S}}^2\right) = V_{\mathrm{Z}}. \tag{4.2}$$

In Fig. 4.1a we present the topological phase diagram as a function of the Zeeman field, V_{Z}, and chemical potential, μ_{S}, calculated according to Eq. (3.10). Indeed, for $\lambda_{\mathrm{F}} \sim 1/m\alpha$ and $L_{\mathrm{S}} = L/3 \ll \lambda_{\mathrm{F}}$, the phase transition follows the line $V_{\mathrm{Z}} = 1/3\sqrt{(\Delta_0^2 + \mu_{\mathrm{S}}^2)}$, marked in red. The green line marks the line $V_{\mathrm{Z}} = \sqrt{(\Delta_0^2 + \mu_{\mathrm{S}}^2)}$, which would have been the topological phase transition if the wire was uniformly covered by a SC, according to Eq. (1.4). The difference between the two lines represents the enlargement of the topological section in parameter space, due to the reduced averaged chemical and induced pairing potentials in the case of the SC lattice. μ_{S} is by assumption and in practice larger than the threshold value of $\sqrt{V_{\mathrm{Z}}^2 - \Delta_0^2}$, which is required in order to achieve a topological phase in a wire uniformly covered by a SC which induces a coupling Δ_0. Furthermore, μ_{S} is hard to control due to the above described gating issues caused by the proximity to the SC . An attempt to reach the topological phase by increasing V_{Z} might suppress the superconductivity, as the critical field of the SC may be reached. The factor of $r < 1$, that appears in Eq. (4.2) due to the periodic application of the SC onto the wire, allows the system to be brought into the topological phase for weaker magnetic fields and for higher values of μ_{S}, as is clearly demonstrated in Fig. 4.1a.

The "price" of this accomplishment, comes in the form of a reduction in the size of the gap protecting the Majorana bound states. For an effective pairing potential of $\bar{\Delta} = r\Delta_0$, we expect the a gap of about $\bar{\Delta}$ far enough from the phase transition

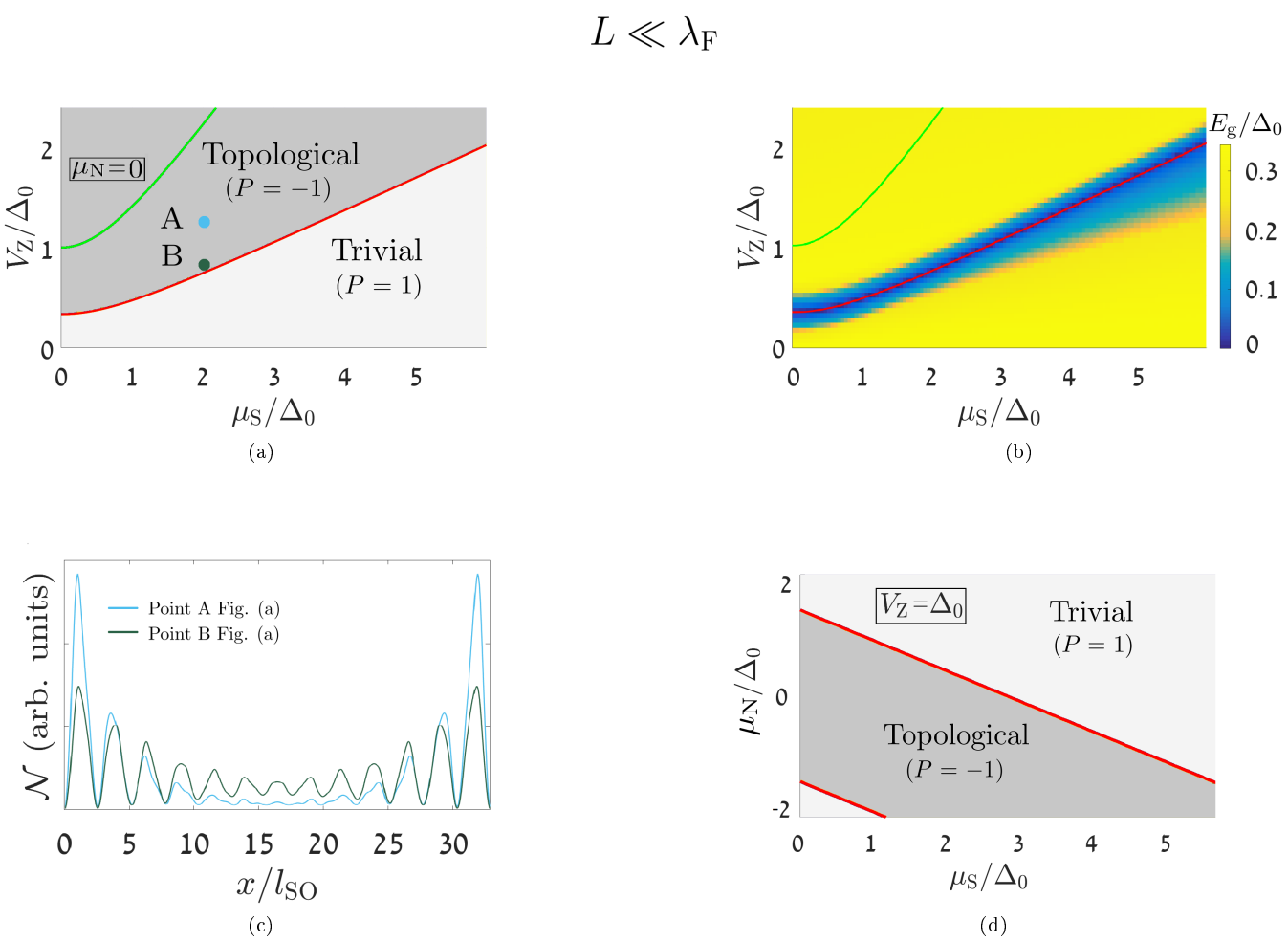

Figure 4.1: Results for a one-dimensional system such as depicted in Fig. 3.1a, in the limit $L \ll \lambda_F$, exemplifying that a topological SC phase with Majorana bound states localized at the system's ends can be reached for a system in proximity to a SC lattice. (a) The topological invariant P as a function of the Zeeman field, V_Z, and the chemical potential of the SC regions, μ_S, calculated according to Eq. (3.10), for $L \sim \lambda_F/100$, $L_S = L/3$ and $E_{SO} = 1.5\Delta_0$. This ratio between E_{SO} and Δ_0 is in accordance with Ref. [12]. The Fermi wavelength, λ_F, was calculated according to Eq. (3.4) [40]. The topological $P = -1$ region is marked in dark grey and the trivial $P = 1$ region is marked in light grey. The phase transition line is marked by the red line. As expected in this $L \ll \lambda_F$ limit, the phase transition follows that of a uniform distribution with modified effective parameters $\bar{\mu} = r\mu_S$ and $\bar{\Delta} = r\Delta_0$, given by Eq. (4.2) with $r = L_S/L = 1/3$. The green line follows Eq. (1.4) and represents the phase transition line for a case where the system is uniformly covered by a SC. An extension of the topological region into lower zeeman fields and higher values of the chemical potential due to the SC lattice is observed. (b) The excitation energy gap normalized by Δ_0. As expected, the gap closes at the phase transition between the trivial and topological phases. The gap in the topological phase far enough from the phase transition line has the expected [41] diminished value of approximately $E_g = r\Delta_0$ due to the SC lattice. (c) The LDOS of the states inside the gap in arbitrary units, calculated according to Eq. (3.19). A tight-binding simulation was used, of a finite wire of length $30 \cdot l_{SO}$, where the spin-orbit coupling length was calculated according to Eq. (3.23). The SC lattice unit cell size was taken to be $L \simeq l_{SO}$ and the fraction covered by a SC was kept at $L_S = L/3 \ll \lambda_F$. The LDOS is shown for two points marked in Fig. (a). Light blue represents point A: $(\mu_S = 2\Delta_0, V_Z = 1.2\Delta_0)$, located well above the phase transition line where the gap is approximately $\bar{\Delta}$, while dark green is for point B: $(\mu_S = 2\Delta_0, V_Z = 0.8\Delta_0)$ which lies close to the phase transition where the gap (shown in Fig. (b)) is small. One observes Majorana bound states, localized at the ends of the system. The localization length of the Majorana states is smaller when the gap is larger, as expected. As can be seen in Fig. (a), for both these points a system uniformly covered by a SC would have been in the trivial phase. (d) The topological invariant P, as a function of the chemical potential in the normal and SC regions, μ_N and μ_S, for $L \sim \lambda_F/15$, $L_S = L/3$. λ_F was calculated according to Eq. (3.24). The phase transition line clearly follows Eq. (4.3) with $r = 1/3$, which is marked by the red line. Note, that since μ_N is tunable we are able to obtain the topological phase even when $\mu_S > \mu_C$.

line [41]. The simulation presented in Fig. 4.1b shows that this is indeed the case. Fig. 4.1c shows the tight-binding simulation for a system with open boundary conditions (see section 3.2). The LDOS of the states inside the gap is shown for two points marked in Fig. 4.1a, with the Majorana bound states clearly visible at the edges of the wire. Both points are located between the red and the green lines in Fig. 4.1a, meaning that for these parameters a system uniformly covered by a SC would have been in the trivial phase.

In order to investigate the effect of the gate potential, we assume that only μ_{N} is affected by it. In the $L \ll \lambda_{\mathrm{F}}$ limit, changing μ_{N} would mean altering the effective chemical potential according to Eq. (4.1). Within the approximation of the effective parameters and for a given unchangeable μ_{S}, one can reach the topological phase when tuning μ_{N} to the region:

$$\frac{r}{1-r}\left(-\mu_{\mathrm{S}}-\sqrt{\left(\frac{V_{\mathrm{Z}}}{r}\right)^{2}-\Delta_{0}^{2}}\right)<\mu_{\mathrm{N}}<\frac{r}{1-r}\left(-\mu_{\mathrm{S}}+\sqrt{\left(\frac{V_{\mathrm{Z}}}{r}\right)^{2}-\Delta_{0}^{2}}\right). \tag{4.3}$$

Fig. 4.1d shows, for a system with periodic boundary conditions, that by bringing down μ_{N} with a gate potential one can compensated for high μ_{S}, when $L \ll \lambda_{\mathrm{F}}$. This is simply due to the fact that the resultant effective potential upholds $\bar{\mu}^2 < V_Z^2 - \bar{\Delta}^2$.

4.1.2 Results for $L \gtrsim \lambda_F$

The picture in the $L \ll \lambda_{\mathrm{F}}$ limit is neatly mapped into a solved uniform problem, with the super-lattice affecting the values of the effective parameters $\bar{\mu}$ and $\bar{\Delta}$. However, in many practical systems, the relevant length scales for the unit cell shown in Fig. 3.1a are λ_{F} and above. For unit cell size in the order of or larger than the Fermi wavelength, $L \gtrsim \lambda_{\mathrm{F}}$, the dependence does not follow Eq. (4.2) perfectly. Instead, an interesting mini-band effect takes place. Since L is large with respect to the Fermi wavelength, the additional momentum bands due to the super-lattice are closer than k_{F} to the original band at $k = 0$. Therefore, in general there are avoided crossings between bands in energies smaller than or equal to the Fermi energy E_{F}.

In this case, the mini-bands created by the super-lattice cannot be ignored. Thus, we use a tight binding simulation rather than the approximation of Eq. (3.10) that was used in some parts of the previous section. Fig. 4.2 presents the phase diagrams for the case $L \sim \lambda_F$ and for the case $L \sim 5\lambda_F$. The mini-bands effect is visible in the higher chemical potentials, as they generate topological $P = -1$ regions for chemical potentials μ_{S} much higher and Zeeman fields much lower than required in the condition given in Eq. (4.2). This creates an interesting situation in which a super lattice with a unit cell of a larger size relative to the case discussed in section 4.1, seemingly grants access to the topological phase for more realistic μ_{S} values, which are much larger than the required for the known uniform case phase transition.

It is important to note that these higher bands are not the transverse sub-bands that become relevant when the cross section of the one-dimensional system is not small enough. They appear even if only one transverse channel is taken into consideration, and as mentioned are created by the super-lattice.

Observing the gap of the systems given in Figs. 4.2b and 4.2d, it can be seen that the gap protecting the Majorana bound states at the high chemical potential topological regions is somewhat diminished. It is also clear that an effort to reduce the size of the unit cell is important even in this regime. we can see that since less mini-bands are compressed into an energy window for $L \sim \lambda_{\mathrm{F}}$ versus $L \sim 5\lambda_{\mathrm{F}}$, the topological regions due to the mini-bands are more extended and robust in the first case. Accordingly, a larger energy gap protecting the Majorana bound states is observed in this case. This result can be further explained by the following argument. Qualitatively speaking, the localization length of the Majorana bound state must be at least the size of a SC lattice unit cell for it to be affected by all the potentials of the SC lattice. When this unit cell increases in length, the minimal Majorana localization length increases with it. As the pairing potential is inversely proportional to the Majorana localization length, one can expect a reduction in the gap when increasing the unit cell size.

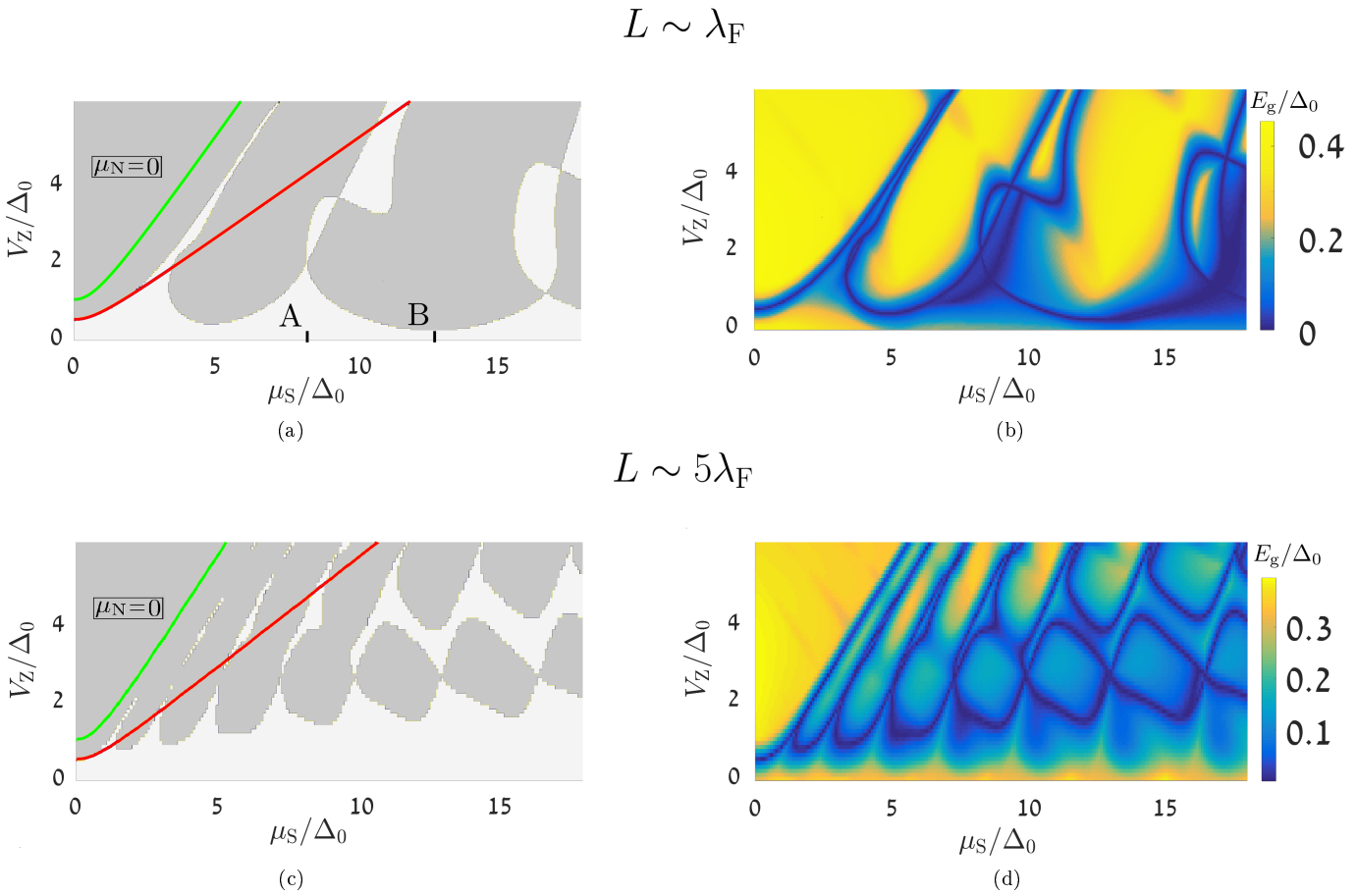

Figure 4.2: Results for a one-dimensional system in proximity to a SC lattice, as depicted in Fig. 3.1a, in the $L \gtrsim \lambda_F$ limit. In this limit, approximations used to derive Eq. (3.10) are invalid so a tight-binding simulation (see section 3.2) was used instead. (a) The topological invariant P as a function of the Zeeman field, V_z, and the chemical potential of the SC regions, μ_S, calculated according to Eq. (3.28), for $L \sim \lambda_F$, $L_S = L/2$ ($r = 1/2$), and $E_{SO} = 1.5\Delta_0$. The Fermi wavelength, λ_F, was calculated according to Eq. (3.24) [40]. Topological ($P = -1$) regions are marked by dark grey and trivial ($P = 1$) regions are marked by light grey. The additional momentum space bands, created by the periodicity of the system, generate topological regions for chemical potentials and Zeeman fields which are outside the region obtained by the uniform approximation of Eq. (4.2), marked in red. (b) The excitation energy gap in units of Δ_0, for $L \sim \lambda_F$ and $L_S = L/2$. In the $L \ll \lambda_F$ limit a gap of about $r\Delta_0$ was obtained in the topological regions. In this $L \sim \lambda_F$ case, the gap remains quite close to this value for $r = 1/2$ in the presented mini-bands. (c) The topological phase diagram as a function of V_Z and μ_S, calculated according to Eq. (3.28), for $L \sim 5\lambda_F$, $L_S = L/2$, and $E_{SO} = 1.5\Delta_0$. In this limit, the topological regions, caused by the additional momentum-space bands, appear denser as a function of μ_S. (d) The excitation energy gap in units of Δ_0, for $L > \lambda_F$. It appears that in the topological regions, the gap protecting the Majorana bound states is reduced substantially relative to the $L \sim \lambda_F$ case.

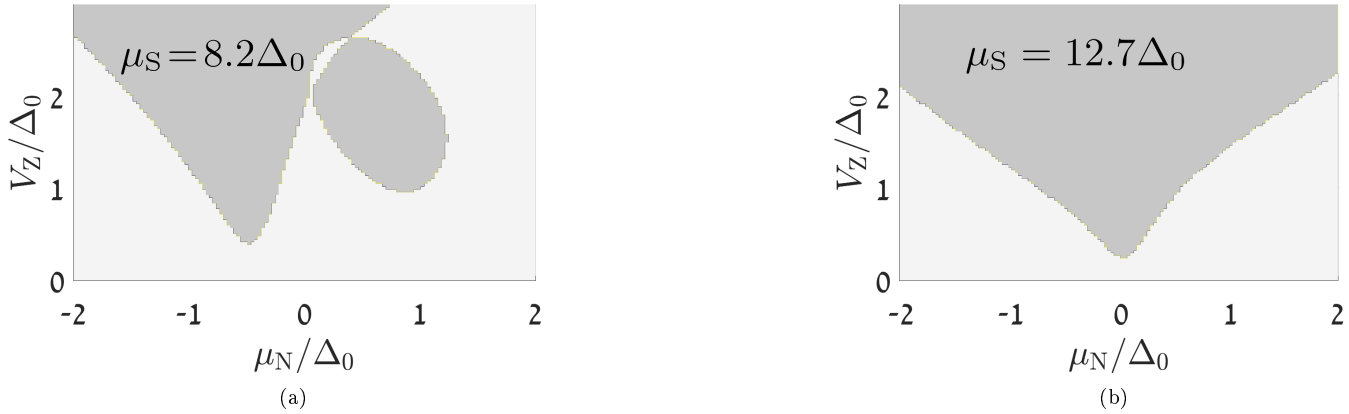

Figure 4.3: The topological invariant P as a function of the experimentally accessible parameters V_Z and μ_N, calculated according to Eq. (3.28), for $L \sim \lambda_F$ [40] and $L_s = L/2$. μ_S is fixed at (a) a "hard" value of $8.2\Delta_0$ (line A in Fig. 4.2a) and (b) an "easy" value of $12.7\Delta_0$ (line B in Fig. 4.2a). As can be seen in Fig. 4.2a, at line A the system is in a region of a trivial phase in parameter space "in between" regions of a topological phase for low and more accessible values of V_Z, while at line B the system can be brought to a topological phase for these values of V_Z. It can be seen that by varying the experimentally accessible parameters μ_N and V_Z, one can reach the topological phase even without the ability to change μ_S, for both situations.

The phase diagram as function of μ_S (shown in Fig. 4.2) is important as this parameter is set by the interface between the SC and the semiconductor, and is often hard to control and limiting. Different values of μ_S, for example lines A and B marked in Fig. 4.2a, can result in different scenarios. For line A ($\mu_S = 8.2\Delta_0$), the system is in a region in parameter space "in between" regions of a topological phase, and a large Zeeman field is required in order to enter the topological phase. For line B ($\mu_S = 12.7\Delta_0$) on the other hand, the system is near a mini-band minimum and can be easily driven into the topological phase for lower more accessible values of the Zeeman field. Interestingly, this occurs despite the fact that $\mu_S^{(A)} < \mu_S^{(B)}$, and it is due to the mini-bands created by the SC lattice.

Assuming that the chemical potential under the SC is hard to control and is unaffected by the gate potential, Fig. 4.3 studies the effect of the experimentally accessible parameters: the chemical potential in the normal regions (controlled by a gate potential) and the Zeeman field (controlled by an external magnetic field). Fig. 4.3a shows that even for the given "problematic" value of μ_S (line A in Fig. 4.2a), one can still reach a topological robust phase when tuning the experimentally accessible parameters.

4.1.3 Spin-Orbit Coupling in the Superconducting Regions Only

We consider a case in which the SOC exists only in the regions covered by a SC, meaning there is no SOC in the non-SC regions. This scenario can resemble the case of a one-dimensional system composed of light chemical elements, such as a Carbon nanotube which has no substantial SOC, covered by a SC lattice composed of a heavy SC such as NbN. Furthermore, this example can serve as a proof of concept for the higher dimensional cases. For example, it serves as an incentive for considering a heavy SC in proximity to a 2DEG with weak SOC, such as GaAs.

In the sites which are not in proximity to a SC, we take the SOC strength to be $\alpha = 0$. For $L \ll \lambda_F$ we expect the

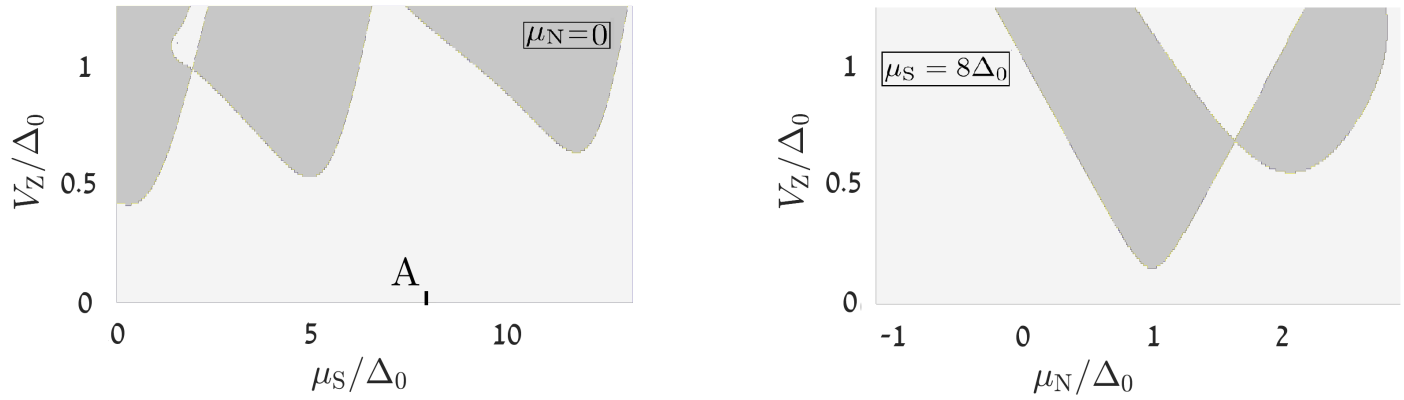

(a) (b)

Figure 4.4: The topological phase diagram for a one-dimensional SC lattice, in which the SOC exists only in regions covered by a SC . In the limit $L \sim \lambda_F$ and for $L_S = \frac{L}{2}$, the topological invariant presented in Eq. (3.28), as a function of (a) μ_S and V_Z for fixed $\mu_N = 0$ and (b) μ_N and V_Z for fixed $\mu_S = 8\Delta_0$. As can be seen in (a), for this value of $\mu_S = 8\Delta_0$ marked by line A, the system is in a region of a trivial phase in parameter space "in between" regions of a topological phase for low and more accessible values of the Zeeman field It can be seen that by varying the experimentally accessible parameters μ_N and V_Z, one can reach the topological phase even without the ability to change μ_S.

electrons would feel a 'smeared' potential, as was exemplified in section 4.1.1. Therefore, this case is less interesting and is expected to yield a topological phase according to Eq. (4.2). Fig. 4.4a shows the phase diagram obtained for $L \sim \lambda_F$. Similar replicas of topological zones in phase space as those analyzed in section 4.1.2 appear at high values of μ_S. Indeed, we see that even in the $L \sim \lambda_F$ regime we receive a topological phase for a SC lattice that has SOC only in regions covered by a SC. The SC lattice scheme also allows us to tune into the topological phase using the gate potential in the normal regions, as is demonstrated in Fig. 4.4b.

4.2 Two-Dimensional Phases

4.2.1 Topological $p_x + ip_y$ Superconducting Phase

We show that a two-dimensional apparatus which involves a SC lattice such as depicted in Fig. 3.1b and described by Hamiltonian of Eq. (3.14) can yield a topological $p_x + ip_y$ SC phase, with propagating zero energy Majorana modes localized at the system's edges. This occurs even when μ_S cannot be brought to the range required in the uniform case according to Eq. (1.12), i.e. when $\mu_S > \mu_C$.

Similarly to the one-dimensional case, we intuitively expect that when the Fermi wavelength of the semiconductor λ_F is much larger than the super-lattice unit cell dimensions, i.e. $L_x, L_y \ll \lambda_F$, the electrons effectively experience 'smeared' potentials. In this limit, $h^x_{\pm 1}$ and $h^y_{\pm 1}$ can be disregarded in Eq. (3.14), and the effective values of the potentials are expected to be their averages presented in Eq. (4.1). The fraction of the unit cell covered by a SC is now given by:

$$r = \frac{L_{Sx} L_{Sy}}{L_x L_y} < 1. \tag{4.4}$$

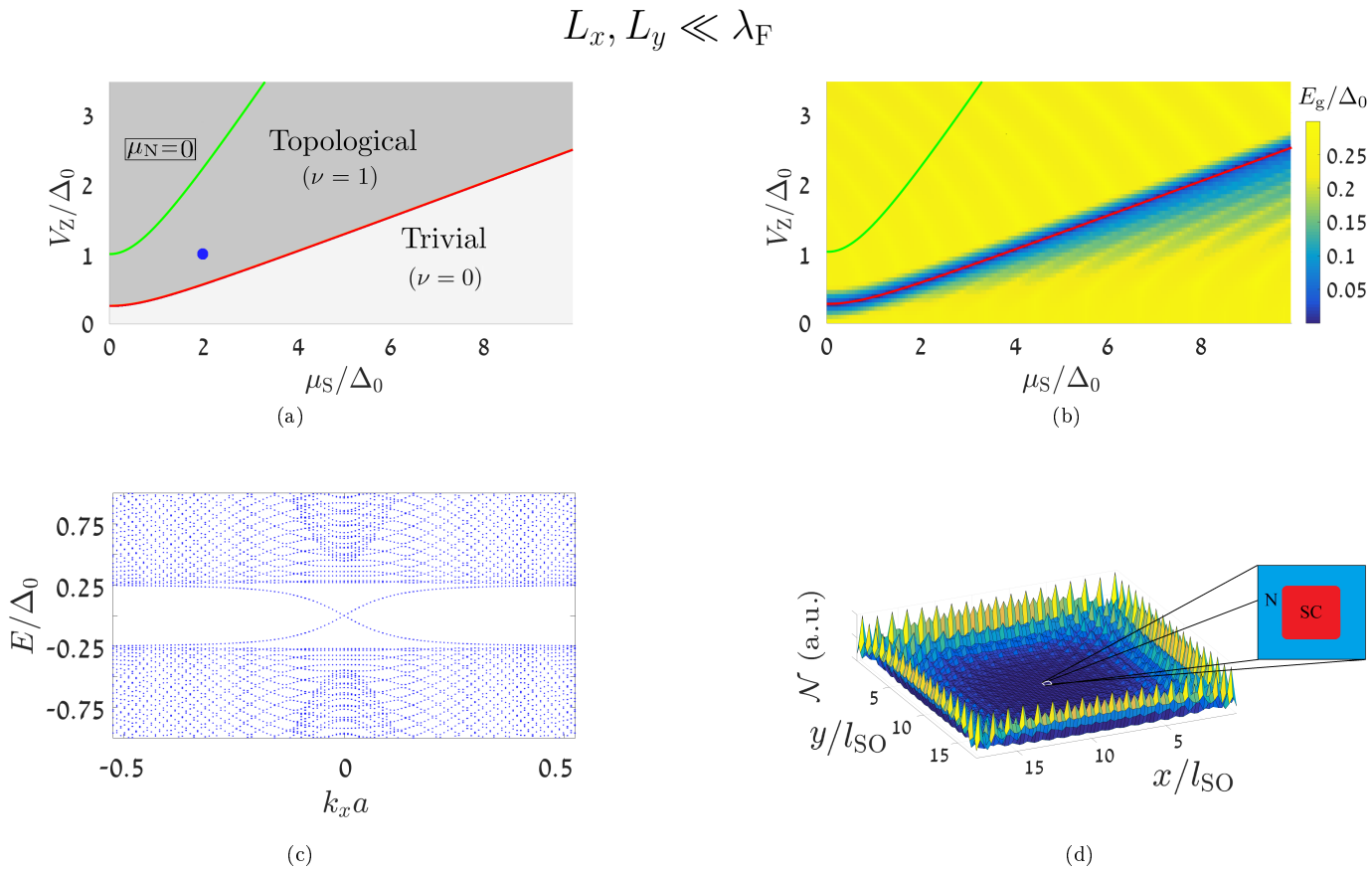

Figure 4.5: Results for $L_x, L_y \ll \lambda_F$ [40] in two dimensions, exemplifying that a topological SC phase with chiral zero energy Majorana modes localized at the system's edges can be reached for a system in proximity to a SC lattice. (a) The Chern number presented in Eq. (3.17), as a function of μ_S and V_Z for $L_x = L_y \sim \lambda_F/100$, $L_{Sx/y} = L_{x/y}/2$ and $E_{SO} = 1.5\Delta_0$. The topological $\nu = 1$ region is marked in dark grey and the trivial $\nu = 0$ region is marked in light grey. The phase transition line, marked by the red line, follows that of a uniform distribution with modified effective parameters $\bar{\mu} = r\mu_S$ and $\bar{\Delta} = r\Delta_0$, given by Eq. (4.5) with $r = L_{Sx}L_{Sy}/L_xL_y = 1/4$. The green line follows Eq. (1.12) and represents the phase transition line for a case where the system is uniformly covered by a SC. (b) Excitation gap normalized by Δ_0, which closes exactly at the phase transition line. The gap in the topological phase has a value of about $E_g = r\Delta_0$. Small oscillations observed in the gap are due to finite size effects. (c) The spectrum as a function of k_x for a two-dimensional tight-binding model with lattice constant a and open boundary conditions in the $\hat{y}$ direction, with $Ls_{x/y} = L_{x/y}/2 \ll \lambda_F$ at the point $(\mu_S = 2\Delta_0, V_z = \Delta_0)$, marked in blue in Fig. (a). The gapless and chiral Majorana edge states are visible at the center of the spectrum, separated by a gap of approximately $r\Delta_0$ from the bulk states. As can be seen in (a), for these parameters a system uniformly covered by a SC would have been in the trivial phase. (d) The LDOS (at zero energy) of the states inside the gap in arbitrary units for the same parameters (blue point in Fig. (a)), with open boundary conditions. A sample size of about $18l_{SO} \times 18l_{SO}$ was taken. The SC lattice unit cell size was taken to be $L_{x/y} \simeq l_{SO}$, and its size is marked and expanded. One observes an enhanced LDOS at the edges, due to the localized Majorana edge state.

Using the values of $\bar{\Delta}$ and $\bar{\mu}$ for $\mu_{\mathrm{N}} = 0$, the phase transition is expected to occur at:

$$r^2\left(\Delta_0^2 + \mu_{\mathrm{S}}^2\right) = V_{\mathrm{Z}}^2. \tag{4.5}$$

Observing Fig. 4.5a, Eq. (4.5) fits perfectly in the limit $L_x, L_y \ll \lambda_F$. As in the one-dimensional case, the topological region in parameter space is expanded to more accessible regions, namely lower Zeeman fields and higher values of μ_{S}, due to the reduction of the effective pairing potential by a factor of r. Fig. 4.5b shows that the gap for excitations is about $\bar{\Delta} = r\Delta_0$, a consistent reduction in the gap protecting the topological phase [41].

Figs. 4.5c and 4.5d show momentum space and real space signatures of the chiral Majorana edge states localized at the system's edges. Fig. 4.5c shows the spectrum as a function of k_x for open boundary conditions in the $\hat{y}$ direction. The gapless chiral Majorana edge states are visible at the center of the spectrum, and the bulk states exhibit a gap of approximately $r\Delta_0$. Fig. 4.5d shows the LDOS of the states inside the gap with open boundary conditions. One observes an enhanced LDOS at the edges, due to the localized Majorana edge state. Both these signatures are shown for the blue point located between the red and the green lines in Fig. 4.5a, meaning that for the same parameters a two-dimensional system uniformly covered by a SC would have been in the trivial phase.

Fig. 4.6 shows results for the more realistic case of a unit cell size of the order of or larger than the Fermi wavelength, $L_x, L_y \gtrsim \lambda_{\mathrm{F}}$. In this case, the dependence does not follow Eq. (4.5) perfectly. Fig. 4.6a shows a multi-band effect similar to the one-dimensional case. Fig. 4.6b shows the gap of the system, which is somewhat diminished due to interference effects. As argued in the one-dimensional case (see full discussion in section 4.1.2), the localization length of the Majorana edge state must be at least the size of a unit cell for it to be affected by all the potentials of the SC lattice. Thus, for a larger size of the SC lattice unit cell, the minimal Majorana localization length is larger, and a decrease in the gap is expected. Even with this decrease, the mini-bands due to the SC lattice are still observed, providing a realistic way to tune into the topological phase when μ_{S} is unmovable.

In Fig. 4.6c, we observe a situation where the chemical potential under the SC falls in a trivial zone between two topological zones for the low and more accessible values of the Zeeman field (line A in Fig. 4.6a). We see that varying the chemical potential in the normal regions, which is an experimentally accesble knob due to the distance from the SC, allows us to tune into the topological phase. Fig. 4.6d shows the momentum space signature of the propagating Majorana edge state, for point B in Fig. 4.6a, which is located in a topological region created by the SC lattice.

4.2.2 Gapless Topological Superconducting Phase

An additional two-dimensional phase we discuss in the context of a SC lattice, is the gapless topological SC phase presented by Baum *et al.* [24]. We first suggest a simple realization setup for this phase, and then move on to combine it with a SC lattice for an achievable gating scheme. It is noteworthy, that our study of this phase is a matter of ongoing research. This section is meant to present our suggested setup and current results, as well as to demonstrate how the SC lattice scheme aids the gating procedure even in the gapless case.

We show that signatures of this phase can be obtained by electing an in-plane magnetization term ($\hat{d} = \hat{y}$) in Eq. (3.11). This term can be experimentally achieved by applying an in-plane magnetic field, which yields no consequent orbital effects. We show the emergence of signatures for the gapless topological SC phase by writing Eq. (3.11) in momentum space, first for uniform $\Delta(\vec{r}) = \Delta_0$ and $\mu(\vec{r}) = \mu_0$:

$$\begin{gathered} H = \int d^2k \Psi_{\vec{k}}^{\dagger} H_{\vec{k}} \Psi_{\vec{k}} \\ H_{\vec{k}} = \left(\tfrac{k^2}{2m} - \mu_0 - \alpha(k_x\sigma_y - k_y\sigma_x)\right)\tau_z + V_{\mathrm{Z}}\sigma_y + \Delta_0\tau_x. \end{gathered} \tag{4.6}$$

The spectrum of this system is gapped for $|V_{\mathrm{Z}}| < |\Delta_0|$, and is gapless for all $|V_{\mathrm{Z}}| \geq |\Delta_0|$. In the latter case, the spectrum exhibits two Dirac cones appearing at opposite momenta and opposite energies, as can be seen in Fig. 4.7a. When adding

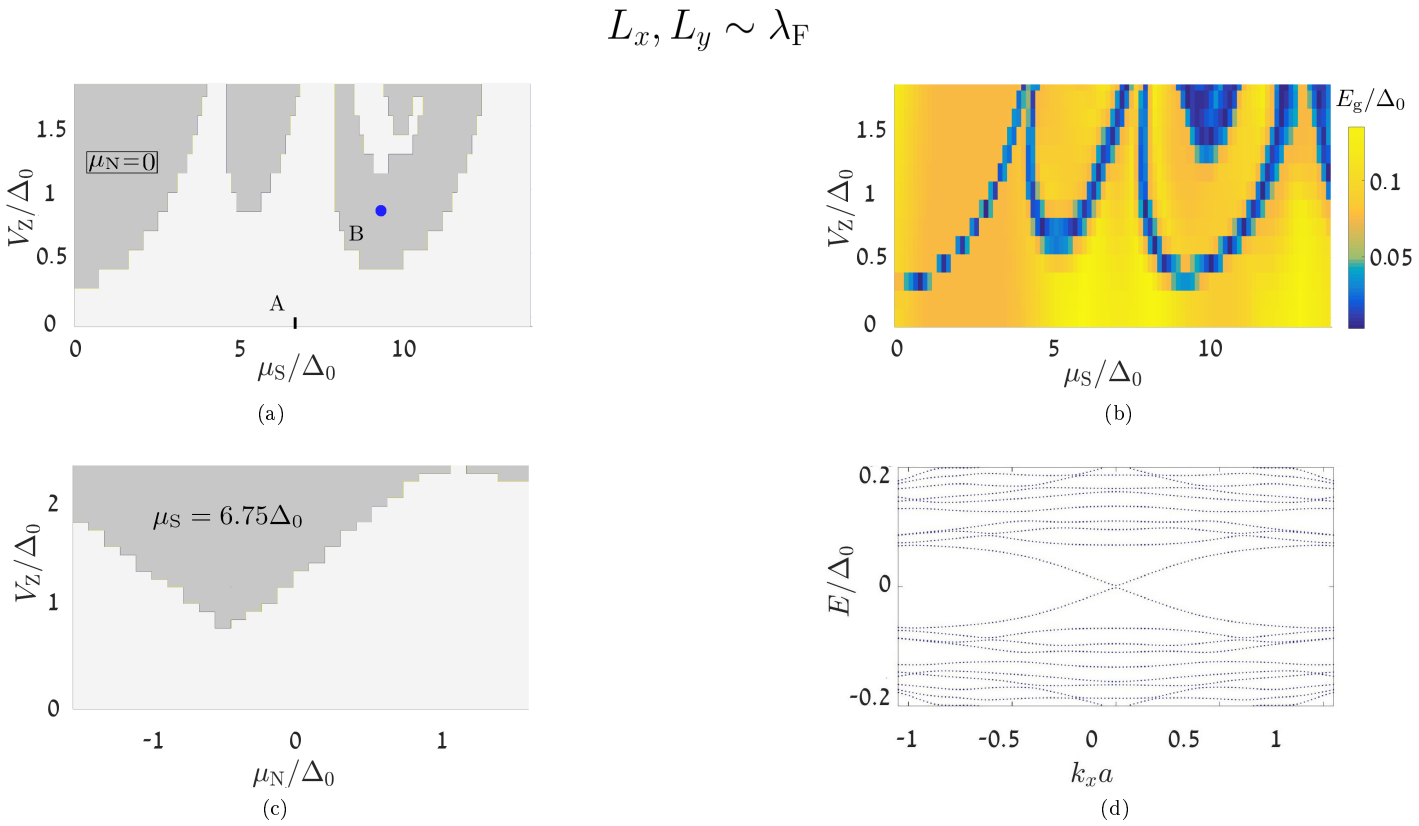

Figure 4.6: Results for $L_x, L_y \sim \lambda_F$ [40] in two dimensions, exemplifying that in this limit as well, a two-dimensional topological SC phase can be reached for a system in proximity to a SC lattice. Furthermore, similarly to the $L \sim \lambda_F$ in the one-dimensional case (Fig. 4.2), a mini-band effect is observed, enabling access to the topological phase for higher values of μ_S and lower values of V_Z than Eq. (4.5) dictates. (a) The Chern number presented in Eq. (3.17), as a function of μ_S and V_Z for $L_x = L_y \sim \lambda_F$, $L_{Sx/y} = L_{x/y}/2$ and $E_{SO} = 1.5\Delta_0$. The topological $\nu = 1$ region is marked in dark grey and the trivial $\nu = 0$ region is marked in light grey. The mini-band effect is evident in two dimensions as well. (b) Excitation gap normalized by Δ_0, which is somewhat diminished due to interference effects. (c) The Chern number as a function of μ_N and V_Z for fixed $\mu_S = 6.75\Delta_0$ (line A marked in Fig. (a)). As can be seen in (a), for this value of μ_S the system in a region of a trivial phase in parameter space "in between" regions of a topological phase for low and more accessible values of V_Z. It can be seen that by varying the experimentally accessible parameters μ_N and V_Z, one can reach the topological phase even without the ability to change μ_S. (d) The spectrum as a function of k_x for a two-dimensional tight-binding model with $L_{Sx/y} = L_{x/y}/2 \sim \lambda_F$, lattice constant a and open boundary conditions in the $\hat{y}$ direction. The spectrum is calculated at the point $\mu_S = 9.35\Delta_0$ and $V_z = 0.95\Delta_0$ (point B marked in Fig. (a)). As can be seen in (a), this point is in a topological region generated by the minibands. The chiral Majorana edge states are visible at the center of the spectrum, not exactly at zero energy due to finite size effects.

an edge perpendicular to the direction of the magnetization, gapless localized edge modes appear which coexists with a gapless bulk, as can be seen in Fig 4.7b. Their protection stems from momentum and energy conservation, and pictorially from the observed separation in k-space between the bulk states and the edge states of the same energies. Even though the bulk is not gapped, an enhanced LDOS is expected near the edges.

Unlike the realization model presented in [24], which uses a modulated magnetization in the perpendicular direction, the band structure for this model is inherently tilted due to the in-plane magnetization. This implies that edge modes located on the two opposite facets of the two-dimensional sample (see Fig. 4.7c), always have the same sign of net velocity. This result is consistent with the system being gapless, since at the edges of the sample translational invariance is broken and the two modes mix with the gapless bulk. It is noteworthy that due to this tilt no small perturbation can render the spectrum fully gapped at a certain energy.

Observing Fig. 4.7b, it is evident that for this phase too there is a requirement regarding the value of the chemical potential. Specifically, we can see that in order to have an edge coexistent with a gapless bulk, the chemical potential must reside between the two cones. The exact values of the cones' locations are easily achievable numerically by digonalizing Eq. (4.6), however their form is quite complex since their existence depends on non-zero Zeeman and SOC terms. In the example shown in Fig. 4.7b, where $V_{\mathrm{Z}} = 1.7\Delta_0$ and $\alpha = 3\sqrt{\Delta_0/m}$, the chemical potential allowing this gapless phase is roughly $|\mu| < 0.4 \cdot \Delta_0 \equiv \mu_{\mathrm{C}}$. This requirement naturally brings forth the SC lattice as a realizable platform for achieving this phase. Figure 4.7d shows the normalized LDOS at zero energy and zero momentum of a system described by the Hamiltonian in Eq. (3.11) with in plane magnetization and a SC lattice with dimensions $Ls_{x/y} = \frac{L_{x/y}}{2}$, and parameters $\mu_{\mathrm{N}} = 0$, $\mu_{\mathrm{S}} = 2\mu_{\mathrm{C}} > \mu_{\mathrm{C}}$. It is evident that even though the bulk states are present at zero energy, the edge states are dominant. The signatures for this two-dimensional gapless topological phase are obtained by covering the 2DEG with a SC lattice, even when assuming the chemical potential under the SC is not in the desired regime.

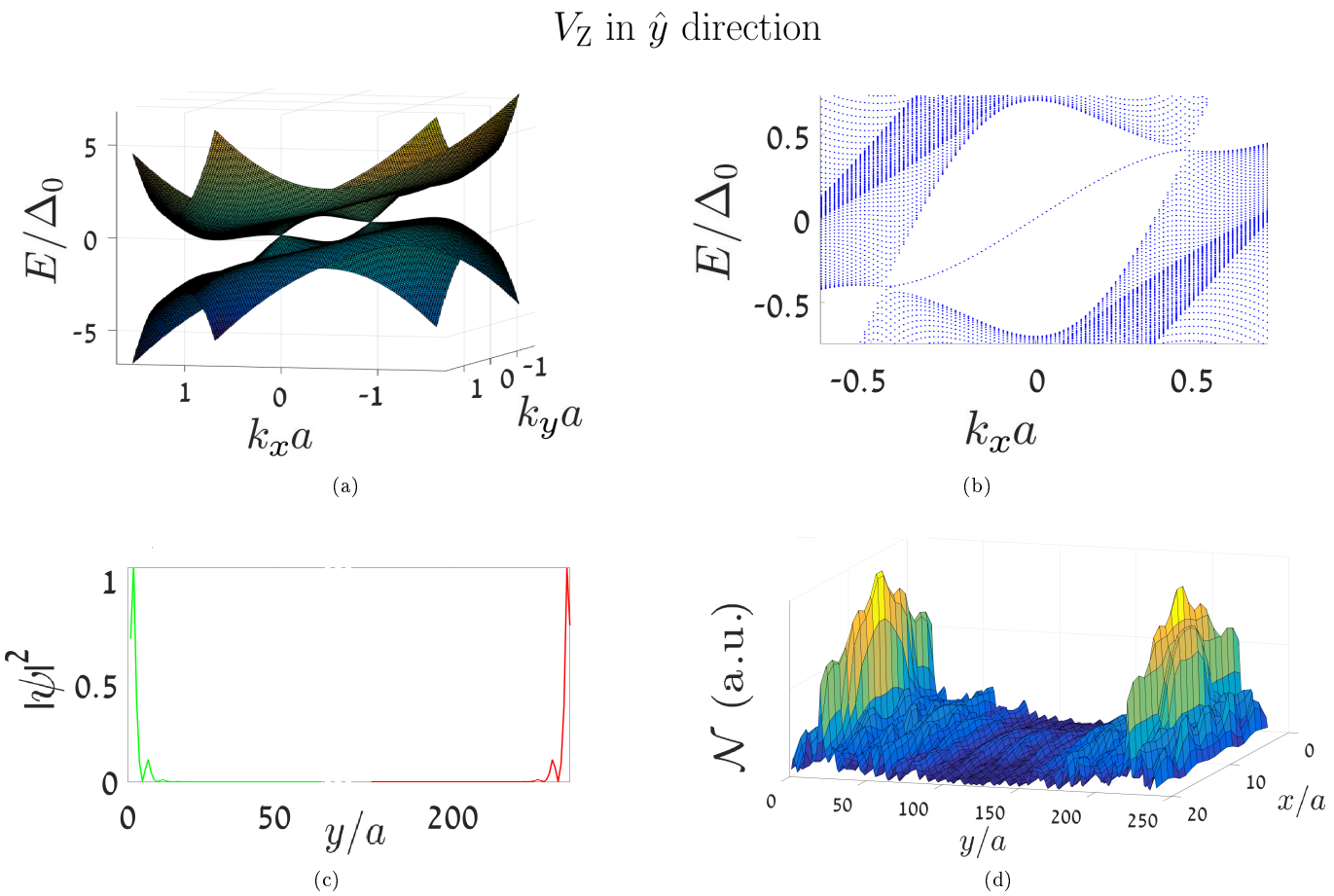

Figure 4.7: Signatures for the gapless topological SC phase appear when applying in-plane magnetization to a 2DEG with SOC in proximity to an s-wave SC. (a) A tilted two-dimensional spectrum, exhibiting two Dirac cones which appear at opposite momenta and opposite energies. This is the form of the spectrum for all $V_z \geq \Delta_0$. Increasing V_z results in an increase in the tilt. (b) An addition of a hard edge perpendicular to the direction of the magnetization results in the appearance of two gapless edge modes within the bulk states window. The two modes overlap in energy almost completely, as their spatial overlap is effectively zero. Due to the tilt caused by the in-plane magnetization term, the two modes always have the same sign of net velocity. (c) A plot of the spatial distribution of the two modes that appear, revealing they are localized on the two opposite edges. (d) A two-dimensional tight-binding simulation with lattice constant a, open boundary conditions in the $\hat{y}$ direction, and periodic boundary conditions in the $\hat{x}$ direction. The LDOS at zero energy and zero momentum is shown, for a system described by the Hamiltonian in Eq. (3.11) with in plane magnetization. The SC lattice has dimensions $L_{\mathrm{S}x/y} = L_{x/y}/2$, and the chemical potential profile is $\mu_{\mathrm{N}} = 0$, $\mu_{\mathrm{S}} = 2\mu_{\mathrm{C}} > \mu_{\mathrm{C}}$. The Zeeman field is $V_z = 1.7\Delta_0$ and the SOC strength is $\alpha = 3\sqrt{\Delta_0/m}$. Each unit cell is of dimension $L_{x/y} = 20a$, and we concatenated 12 unit cells in the $\hat{y}$ direction while setting periodic boundary conditions in the $\hat{x}$ direction. It is evident the edge states are present when covering the 2DEG with a SC lattice, even when assuming the chemical potential under the SC is not in the energy-momentum "window" shown in Fig. (b). Setting periodic boundary conditions in the $\hat{y}$ direction while concatenating 12 unit cells in the $\hat{x}$ direction, we receive no enhanced LDOS near the edge parallel to the $\hat{y}$. This corresponds to rotation of the in-plane magnetic field by 90 degrees, which should create or annihilate the localized states on a specific edge.

Chapter 5

Experimental Apparatuses

5.1 One-Dimensional Superconducting Phase

5.1.1 Realization in Wires

We have established that a one-dimensional SC lattice such as described in section 3.1.1 results in spatially separated zero energy Majorana end states. One can imagine realizing this phase by periodically covering a one-dimensional nanowire with an s-wave SC from atop. This would be in accordance with the majority of current realization schemes, which cover the nanowire with a uniform layer of a SC. We suggest an alternative version, depicted in Fig. 5.1, where the wire is placed on top of a SC in the shape of a comb. This apparatus, allows one to measure the LDOS of the Majorana states, such as the one we have shown in Fig. 4.1c, using a scanning tunneling microscope (STM). The STM tip could access the wire from atop, without the obstruction of the SC.

A caveat to this approach, is the fact that the screening by the SC in the regions it does exist in the comb geometry, would be total, rendering the gate's affect on the chemical potential negligible in these regions. Indeed, without the use of the SC lattice geometry, it makes more sense to cover the nanowire with the SC from atop in order to reduce the screening effects. In addition, in this configuration, as the wire is placed on top of the SC which tends to oxidize easily, one has to make sure that a good contact between the wire and the SC is established.

Using the SC lattice geometry, we have demonstrated that a SC topological phase can be reached even in the worst case of no control over the chemical potential in regions covered by a SC. The gating in the normal regions is sufficient in order to tune into the topological phase. Thus, our suggestion, which is based on the SC lattice geometry, allows measuring the LDOS of an entire topological wire directly with an STM.

5.1.2 Realization in 2DEGs and Braiding

Alternatively to the nano-wire based realization, one can attempt to use a one-dimensional channel which resides within a two-dimensional environment, for example a 2DEG. This scheme is beneficial twice. Firstly, the fabrication process of a 2DEG usually results in samples much cleaner than the one-dimensional nanowires, where the effect of disorder often dominates. The effective induced SC gap, Δ_{eff}, protects the topological phase in the presence of disorder of typical energy E_{dis}, as long as $\Delta_{\text{eff}} > E_{\text{dis}}$. If one were to construct the one-dimensional phase within a two-dimensional sample, the Majorana states could be well protected even if the effective induced SC gap is relatively small. Secondly, within the

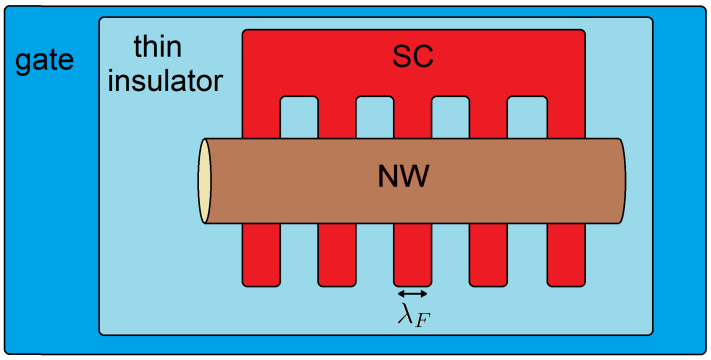

Figure 5.1: Suggested SC lattice based realization scheme for the one-dimensional topological SC phase discussed in section 3.1.1. The wire is placed *above* a SC in the shape of a comb, while its top can be measured with an STM without the obstruction of a SC. The gating form in this case would be similar to the model analyzed above, which was shown to be in the topological regime even if the chemical potential under the SC strips is completely unaffected by the external gate. The comb geometry ensures that the SC strips are connected and shorted, so that all the SC in contact with the wire have the same phase.

framework of this two-dimensional realization, a Majorana braiding procedure which utilizes the periodic nature of the SC lattice can be employed.

We begin by picturing a one-dimensional SC lattice such as the one analyzed in section 3.1.1, set up within a one-dimensional channel in a two-dimensional sample. The two-dimensional sample can be a 2DEG made from a material with strong SOC, such as InAs or InSb. The one-dimensional channel can be obtained for example by using a top-gate which depletes a specific part of the 2DEG.

In Fig. 5.2 we see an illustration of such a one-dimensional SC lattice residing within a two-dimensional sample. Assume that without gating, the one-dimensional system we can refer to as the "wire" is initially in a trivial phase. Assume that we are in an operating point which corresponds to line A in Fig. 4.2a, such that if the chemical potential in the normal regions is tuned by gating to $\mu_N = -0.5\Delta_0$, the "wire" would enter a topological phase when a Zeeman field of $V_Z = \Delta_0$ is applied, as can be seen in Fig. 4.3a. Alternatively, if our operating point corresponds to line B in Fig. 4.2a, gating μ_N to 0 would result in a topological "wire" when a Zeeman field of $V_Z = \Delta_0$ is applied, as can be seen in Fig. 4.3b. Now, as is portrayed in Fig. 5.2, we can think of gating the normal regions to the correct value for a gradually increasing amount of unit cells (the assumption throughout this paper is that μ_N is the tunable parameter while μ_S is not). As is pictorially demonstrated, this procedure results in an effective topological "wire", with a gradually increasing effective length implying a gradually decreasing overlap between Majorana end modes.

For practical experimental realizations, it is desirable that the Majorana localization length will be small enough in terms of the SC lattice unit cells. Fig. 5.3 shows an example for $L \sim \lambda_F$, in which the spectrum stabilizes after approximatly 6 unit cells. This means that the Majoranas' overlap becomes negligible after 6 unit cells. Due to the exponential nature of the Majorana wavefunction decay, any number of unit cells greater than 6 is effectively infinity, making the apparatus realizable.

The procedure depicted in Fig. 5.2 and the corresponding spectrum shown in Fig. 5.3, provide us with a measurable signature of this phase. We suggest to measure the spectrum on one end of the effective wire while gradually increasing its length using the gates. This measurement can be preformed via a tunneling barrier at the edge of the 2DEG. The spectrum would reveal a Majorana state gradually decaying to zero energy, as Fig. 5.3 shows. We note that there is a

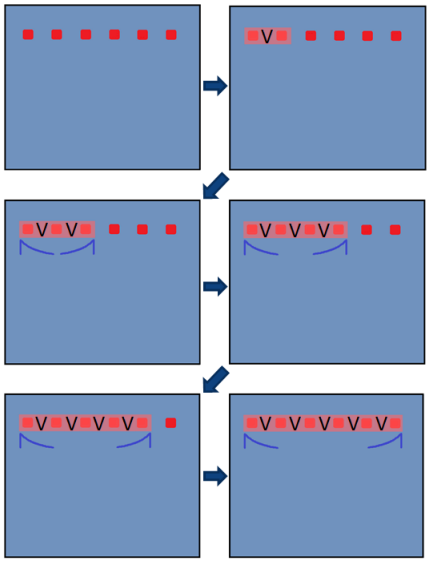

Figure 5.2: An illustration of the process of spatially separating the Majoranas at the edges of the one-dimensional SC lattice. The light blue surface represents the two-dimensional substrate and the dark blue lines represent the decaying envelope of the Majorana wave functions located at the edges of the effective "wire". The amount of unit cells comprising the effective "wire", is controlled by the gates represented by the 'V' symbols, placed between the SC islands, represented by the red squares. Gating the normal regions such that μ_{N} assumes the value required for the topological phase (cf. Fig. 4.3), for an increasing amount of unit cells, results in an effective topological "wire" with a gradually increasing effective length, implying a gradually decreasing overlap between Majorana end modes. If we imagine that the SC islands are connected from above and shorted, similarly to the comb geometry presented in Fig. 5.1, then a measurement of the LDOS on one of the "wire" ends through a tunneling barrier is possible without charging the islands.

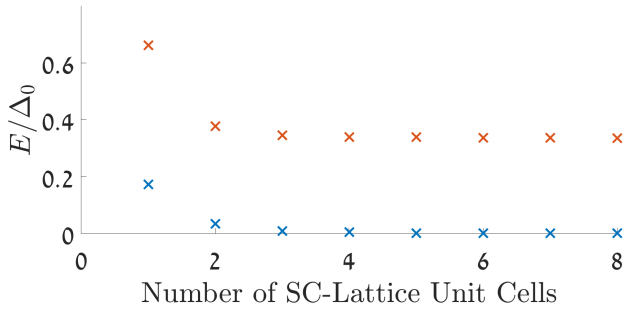

Figure 5.3: The 2 lowest positive energy levels of a one-dimensional system as a function of the number of unit cells in the SC lattice (due to particle-hole symmetry, the spectrum is symmetric around zero). The blue crosses represent the positive energy mode comprised of a pair of majoranas located at the wire's ends. This mode approaches zero energy as the effective wire length increases and the overlap between the Majoranas decreases. The orange crosses, which are the first of the bulk states, represent the gap. The chemical potential under the SC is as usual taken to be larger than the critical value for a wire uniformly covered by a SC, μ_C. The chemical potential in the normal region is tuned to $\mu_N = 0$. The length of a unit cell is $L \sim \lambda_F$, and the SC ratio is $L_S = L/2$. The Zeeman field is $V_Z = 2\Delta_0$. The results show that the Majorana end modes decouple for an approximate length of 6 unit cells and higher, as the gap stabilizes and the Majorana modes are effectively at zero energy.

challenge in gating specific points in the 2DEG, as it requires additional electronic inputs to the circuit, as well as relative precision in the spatial extent of the applied voltage.

Finally, we recall the braiding procedure suggested in Refs. [3, 43], referred to as 'Y-junction' or 'T-junction' braiding, where a sequence of operations decreasing and increasing the overlap between different Majorana pairs in a Y or T geometry was shown to result in an effective Majorana braiding. The SC lattice can be employed for realizing this braiding, as is portrayed in Fig. 5.4. The required tuning of the effective overlap between Majorana pairs can be achieved using local gating between SC islands, effectively increasing and decreasing the length of the "wires".

5.2 Two-Dimensional Superconducting Phases

5.2.1 Topological $p_x + ip_y$ Superconducting Phase

In order to obtain the p_x+ip_y phase described in section 3.1.2.1, we required a Zeeman term in the $\hat{z}$ direction, perpendicular to the 2DEG surface. Ref. [8] suggests achieving this term using a ferromagnetic insulator placed in proximity to the 2DEG. This scheme requires a good interface between the ferromagnetic insulator and the quantum well in order to obtain a sufficiently large value of the Zeeman field, which poses a significant engineering challenge. In addition, this would limit the ability to alter the value of the Zeeman field. If one simply applies an external magnetic field perpendicular to the 2DEG, it is far from obvious that the Zeeman field dominates over orbital effects, which could affect the SC and are beyond the scope of this thesis.

Ref. [20] shows that if one considers a zincblende quantum well grown along the 110 direction, rather than the more common 100 direction, then the application of a parallel magnetic field would drive the system into a topological SC phase. This is shown by considering the Dresselhaus spin-orbit coupling term, which may be significant in InSb quantum wells, as bulk InSb exhibits large Dresselhaus spin-orbit interactions relative to bulk InAs or GaAs [44]. As stated above,

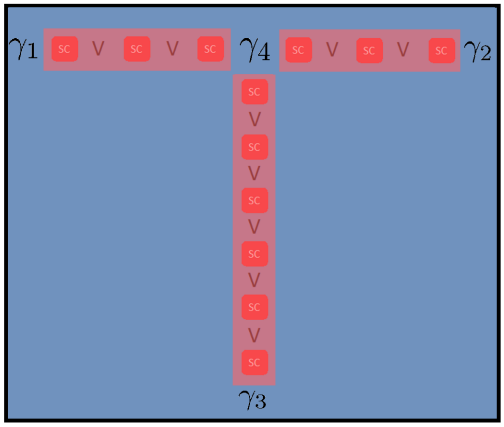

Figure 5.4: An illustration of a T-junction apparatus implemented in a two-dimensional system, comprised of one-dimensional SC lattices which create wires of varying effective lengths. Tuning the effective overlap between Majorana pairs as required for the braiding procedure presented in [3, 43] can be achieved using local gating between SC islands, effectively increasing and decreasing the lengths of the "wires". In this example, Majoranas γ_1 and γ_2 have high overlap with Majorana γ_4. Majorana γ_3 has low overlap with Majorana γ_4, as it is located 6 unit cells away from it (see Fig. 5.3).

orbital effects are expected to be small when applying an in-plane magnetic field. The SC lattice presented in this work offers a practical solution to the gating issue. Combining the SC lattice with the proposal for application of a parallel magnetic field on a 110 well, provides a practical scheme for the realization of the p-wave SC phase in two dimensions.

5.2.2 Gapless Topological Superconducting Phase

For the realization of the gapless topological SC phase, we suggested a simple setup discussed in section 4.2.2. The inherent tilt in the spectrum described above and portrayed in Fig. 4.7(a), facilitates an interesting experimental signature. The presence of this tilt implies that edge modes located on the two opposite facets of the sample always have the same sign of net velocity. Thus, the thermal conductivity measured from one end of the sample to the other, in the direction parallel to the vlocity of both edges, will contain an ingredient of the edges' contribution. This ingredient will have the value of $2g_0$, where $g_0 = \pi^2 k_B^2 T/3h$ is the thermal conductance quantum. Therefore, when we subtract the "upstream" contribution to the thermal conductance from the "downstream" one, the bulk contribution cancels and the net result is expected to be equal to $2g_0$. Alternatively, rotation of the in-plane magnetic field by 90 degrees should create or annihilate the localized states on a specific edge, thus measuring the thermal conductivity on the edge during rotation should reveal or conceal this term. Additionally, a measurement of the LDOS via a tunnel barrier on the edges of the sample, in different orientations of the magnetic field, should show the contribution of the edge states, as is shown in Fig. 4.7(d).

Chapter 6

Discussion

In this work, we have suggested a practical solution in the form of a SC lattice to the problem of gating systems in the vicinity of a SC. We have established that for a SC lattice with a unit cell of size $L \gtrsim \lambda_{\mathrm{F}}$, high energy mini-bands create additional topological regions that reside close to high values of μ_{S} (cf. Figs. 4.2 and 4.6). Importantly, since μ_{S} is set by the system parameters and is more difficult to tune due to screening, these topological regions are accessible by tuning μ_{N} for a large range of μ_{S}.

For $L > \lambda_{\mathrm{F}}$ we have observed a reduction in the gap size. Hence, a SC lattice with $L \sim \lambda_{\mathrm{F}}$ is the optimal choice as it creates topological regions close to the chemical potential that still show robustness due to a relatively large energy gap.

For a SC lattice with a unit cell of size $L \ll \lambda_{\mathrm{F}}$, the system is effectively described by the average values of the chemical and induced pairing potentials. As shown in Figs. 4.1 and 4.5, the topological phase transition is then described by Eq. (4.2) in one dimension and Eq. (4.5) in two dimensions. The SC lattice potential effectively enlarges the topological region and makes it more accessible than the uniform case, as the topological phase can occur at higher chemical potentials under the SC and at lower Zeeman fields.

Furthermore, we suggested a realizable apparatus in which signatures for the gapless topological SC phase can be observed. We demonstrated that in this case as well, a SC lattice renders practical a proposal based on gating a system in proximity to a SC.

Finally, we discussed several experimental configurations containing SC lattices in which the phases described above can be realized, and we have suggested measurable signatures of these phases. Further work should include the investigation of additional SC lattice structures (e.g. honeycomb), effects of an orbital magnetic field that may create vortexes in the SCs, effects of charging energies in the SC islands and effects of electron repulsion in the 2DEG.

Bibliography

[1] Ady Stern. Non-abelian states of matter. *Nature*, 464(7286):187–193, 2010. 1.1

[2] A Yu Kitaev. Fault-tolerant quantum computation by anyons. *Annals of Physics*, 303(1):2–30, 2003. 1.1

[3] Bertrand I Halperin, Yuval Oreg, Ady Stern, Gil Refael, Jason Alicea, and Felix von Oppen. Adiabatic manipulations of majorana fermions in a three-dimensional network of quantum wires. *Physical Review B*, 85(14):144501, 2012. 1.1, 5.1.2, 5.4

[4] Jay D Sau, David J Clarke, and Sumanta Tewari. Controlling non-abelian statistics of majorana fermions in semiconductor nanowires. *Physical Review B*, 84(9):094505, 2011. 1.1

[5] A Yu Kitaev. Unpaired majorana fermions in quantum wires. *Physics-Uspekhi*, 44(10S):131, 2001. 1.1, 3.1.1

[6] Liang Fu and C. L. Kane. Superconducting proximity effect and majorana fermions at the surface of a topological insulator. *Phys. Rev. Lett.*, 100:096407, Mar 2008. 1.1

[7] Liang Fu and C. L. Kane. Josephson current and noise at a superconductor/quantum-spin-hall-insulator/superconductor junction. *Phys. Rev. B*, 79:161408, Apr 2009. 1.1

[8] Jay D. Sau, Roman M. Lutchyn, Sumanta Tewari, and S. Das Sarma. Generic new platform for topological quantum computation using semiconductor heterostructures. *Phys. Rev. Lett.*, 104:040502, Jan 2010. 1.1, 1.3, 1.3, 3.1.2.1, 5.2.1

[9] Roman M. Lutchyn, Jay D. Sau, and S. Das Sarma. Majorana fermions and a topological phase transition in semiconductor-superconductor heterostructures. *Phys. Rev. Lett.*, 105:077001, Aug 2010. 1.1, 4.1.1

[10] Yuval Oreg, Gil Refael, and Felix von Oppen. Helical liquids and majorana bound states in quantum wires. *Phys. Rev. Lett.*, 105:177002, Oct 2010. 1.1, 4.1.1

[11] V. Mourik, K. Zuo, S. M. Frolov, S. R. Plissard, E. P. A. M. Bakkers, and L. P. Kouwenhoven. Signatures of majorana fermions in hybrid superconductor-semiconductor nanowire devices. *Science*, 336(6084):1003–1007, 2012. 1.1, 1.5

[12] Anindya Das, Yuval Ronen, Yonatan Most, Yuval Oreg, Moty Heiblum, and Hadas Shtrikman. Zero-bias peaks and splitting in an Al-InAs nanowire topological superconductor as a signature of Majorana fermions. *Nature Physics*, 8(12):887–895, 2012. 1.1, 4.1

[13] Leonid P. Rokhinson, Xinyu Liu, and Jacek K. Furdyna. The fractional a.c. Josephson effect in a semiconductorâsuperconductor nanowire as a signature of Majorana particles. *Nature Physics*, 8(11):795–799, 2012. 1.1

[14] M. T. Deng, C. L. Yu, G. Y. Huang, M. Larsson, P. Caroff, and H. Q. Xu. Anomalous zero-bias conductance peak in a nbâinsb nanowireânb hybrid device. *Nano Letters*, 12(12):6414–6419, 2012. PMID: 23181691. 1.1

[15] A. D. K. Finck, D. J. Van Harlingen, P. K. Mohseni, K. Jung, and X. Li. Anomalous modulation of a zero-bias peak in a hybrid nanowire-superconductor device. *Phys. Rev. Lett.*, 110:126406, Mar 2013. 1.1

[16] H. O. H. Churchill, V. Fatemi, K. Grove-Rasmussen, M. T. Deng, P. Caroff, H. Q. Xu, and C. M. Marcus. Superconductor-nanowire devices from tunneling to the multichannel regime: Zero-bias oscillations and magnetoconductance crossover. *Phys. Rev. B*, 87:241401, Jun 2013. 1.1

[17] Stevan Nadj-Perge, Ilya K. Drozdov, Jian Li, Hua Chen, Sangjun Jeon, Jungpil Seo, Allan H. MacDonald, B. Andrei Bernevig, and Ali Yazdani. Observation of majorana fermions in ferromagnetic atomic chains on a superconductor. *Science*, 346(6209):602–607, 2014. 1.1

[18] Satoshi Fujimoto. Topological order and non-abelian statistics in noncentrosymmetric s-wave superconductors. *Phys. Rev. B*, 77:220501, Jun 2008. 1.3

[19] Chuanwei Zhang, Sumanta Tewari, Roman M. Lutchyn, and S. Das Sarma. p_x+ip_y superfluid from s-wave interactions of fermionic cold atoms. *Phys. Rev. Lett.*, 101:160401, Oct 2008. 1.3

[20] Jason Alicea. Majorana fermions in a tunable semiconductor device. *Phys. Rev. B*, 81:125318, Mar 2010. 1.3, 1.3, 3.1.2.1, 5.2.1

[21] N. Read and Dmitry Green. Paired states of fermions in two dimensions with breaking of parity and time-reversal symmetries and the fractional quantum hall effect. *Phys. Rev. B*, 61:10267–10297, Apr 2000. 1.3

[22] D. A. Ivanov. Non-abelian statistics of half-quantum vortices in p-wave superconductors. *Phys. Rev. Lett.*, 86:268–271, Jan 2001. 1.3

[23] Jason Alicea. New directions in the pursuit of majorana fermions in solid state systems. *Reports on Progress in Physics*, 75(7):076501, 2012. 1.2

[24] Yuval Baum, Thore Posske, Ion Cosma Fulga, Björn Trauzettel, and Ady Stern. Gapless topological superconductors: Model hamiltonian and realization. *Phys. Rev. B*, 92:045128, Jul 2015. 1.4, 1.4, 1.3, 4.2.2, 4.2.2

[25] SM Albrecht, AP Higginbotham, M Madsen, F Kuemmeth, TS Jespersen, Jesper Nygard, P Krogstrup, and CM Marcus. Exponential protection of zero modes in majorana islands. *Nature*, 531(7593):206–209, 2016. 1.5

[26] Yao Lu, Wen-Yu He, Dong-Hui Xu, Nian Lin, and K. T. Law. Platform for engineering topological superconductors: Superlattices on rashba superconductors. *Phys. Rev. B*, 94:024507, Jul 2016. 1.5

[27] Jay D Sau, Chien Hung Lin, Hoi-Yin Hui, and S Das Sarma. Avoidance of majorana resonances in periodic topological superconductor-nanowire structures. *Physical review letters*, 108(6):067001, 2012. 1.5

[28] Jay D Sau and S Das Sarma. Realizing a robust practical majorana chain in a quantum-dot-superconductor linear array. *Nature communications*, 3:964, 2012. 1.5

[29] Ion C Fulga, Arbel Haim, Anton R Akhmerov, and Yuval Oreg. Adaptive tuning of majorana fermions in a quantum dot chain. *New Journal of Physics*, 15(4):045020, 2013. 1.5

[30] P Zhang and Franco Nori. Majorana bound states in a disordered quantum dot chain. *New Journal of Physics*, 18(4):043033, 2016. 1.5

[31] There are several length scales corresponding to the SOC energy, chemical potentials, pairing potential, and Zeeman energy. In our simulations, and in most relevant cases they all of the same order of magnitude. When comparing the SC lattice unit cell with these length scales, we take λ_{F} to be the representative one. 3.1.1

[32] Since we threw all momentum space replicas except for the ones at $G = 0, \pm 1$, $H(k = \pi/L)$ is only approximately equal to $H(k = -\pi/L)$ when $L \ll \lambda_{\mathrm{F}}$. 3.1.1

[33] Alexander Altland and Martin R. Zirnbauer. Nonstandard symmetry classes in mesoscopic normal-superconducting hybrid structures. *Phys. Rev. B*, 55:1142–1161, Jan 1997. 3.1.1, 3.1.2.1

[34] Andreas P. Schnyder, Shinsei Ryu, Akira Furusaki, and Andreas W. W. Ludwig. Classification of topological insulators and superconductors in three spatial dimensions. *Phys. Rev. B*, 78:195125, Nov 2008. 3.1.1, 3.1.2.1

[35] Alexei Kitaev. Periodic table for topological insulators and superconductors. *arXiv preprint arXiv:0901.2686*, 2009. 3.1.1, 3.1.2.1

[36] The symmetry $\mathcal{T} = \kappa$ is fragile and can be broken easily, leaving the system in the symmetry class D. 3.1.1

[37] Sumanta Tewari and Jay D Sau. Topological invariants for spin-orbit coupled superconductor nanowires. *Physical review letters*, 109(15):150408, 2012. 3.1.1

[38] Parag Ghosh, Jay D Sau, Sumanta Tewari, and S Das Sarma. Non-abelian topological order in noncentrosymmetric superconductors with broken time-reversal symmetry. *Physical Review B*, 82(18):184525, 2010. 3.1.1

[39] Inbar Seroussi, Erez Berg, and Yuval Oreg. Topological superconducting phases of weakly coupled quantum wires. *Phys. Rev. B*, 89:104523, Mar 2014. 3.1.2.1

[40] λ_{F} depends on μ and V_Z, thus its relation to the dimensions of the system (L, L_x etc.) is not constant in the above figures. However, it does remain in the same order of magnitude and in the stated regime. 4.1, 4.2, 4.3, 4.5, 4.6

[41] For $\bar{\Delta} < E_{\mathrm{SO}}$ the gap at $\pm k_{\mathrm{F}}$ is approximately $\bar{\Delta}/\sqrt{1 + \frac{V_Z^2}{4E_{\mathrm{SO}}^2}}$ which is close to $\bar{\Delta}$ for the shown Zeeman field values. It is the actual gap far enough from the phase transition line once the gap at $k = 0$, which closed at the phase transition, increases sufficiently. 4.1, 4.1.1, 4.2.1

[42] Shu-Ping Lee, Jason Alicea, and Gil Refael. Electrical manipulation of majorana fermions in an interdigitated superconductor-ferromagnet device. *Phys. Rev. Lett.*, 109:126403, Sep 2012. 4.1.1

[43] Jason Alicea, Yuval Oreg, Gil Refael, Felix von Oppen, and Matthew PA Fisher. Non-abelian statistics and topological quantum information processing in 1d wire networks. *Nature Physics*, 7(5):412–417, 2011. 5.1.2, 5.4

[44] Roland Winkler. *Spin-orbit coupling effects in two-dimensional electron and hole systems*. Springer tracts in modern physics. Springer, Berlin, 2003. 5.2.1

Chapter 7

Acknowledgments

I would like to express my appreciation and gratitude to my adviser, Prof. Yuval Oreg, for his guidance, support and engagement through the process of this master thesis. Furthermore, I wish to thank Dr. Arbel Haim and Dr. Yuval Baum for their assistance and advice in the innumerable conversations we had during the work process. Additionally, I would like to acknowledge Eyal Leviatan and Yonathan Efroni, who made my experience much more enjoyable. Most importantly, I would like to thank my family. I am grateful for my parents, who with their endless support have enabled me to always reach far. Finally, thank you Gali, my wife, for everything you are to me.